UNIVERSITY OF LEEDS

This is a repository copy of *A branched magma feeder system during the 1669 eruption of Mt. Etna: evidence from a time-integrated study of zoned olivine phenocryst populations*.

White Rose Research Online URL for this paper:
http://eprints.whiterose.ac.uk/116175/

Version: Accepted Version

Article:

Kahl, M, Viccaro, M, Ubide, T et al. (2 more authors) (2017) A branched magma feeder system during the 1669 eruption of Mt. Etna: evidence from a time-integrated study of zoned olivine phenocryst populations. Journal of Petrology, 58 (3). pp. 443-472. ISSN 0022-3530

https://doi.org/10.1093/petrology/egx022

(c) 2017, The Author. Published by Oxford University Press. All rights reserved. For Permissions, please e-mail: journals.permissions@oup.com. This is a pre-copyedited, author-produced PDF of an article accepted for publication in the Journal of Petrology following peer review. The version of record, 'Kahl, M, Viccaro, M, Ubide, T et al (2017) A branched magma feeder system during the 1669 eruption of Mt. Etna: evidence from a time-integrated study of zoned olivine phenocryst populations. Journal of Petrology, 58 (3). pp. 443-472,' is available online at: https://doi.org/10.1093/petrology/egx022

Reuse
Items deposited in White Rose Research Online are protected by copyright, with all rights reserved unless indicated otherwise. They may be downloaded and/or printed for private study, or other acts as permitted by national copyright laws. The publisher or other rights holders may allow further reproduction and re-use of the full text version. This is indicated by the licence information on the White Rose Research Online record for the item.

Takedown
If you consider content in White Rose Research Online to be in breach of UK law, please notify us by emailing eprints@whiterose.ac.uk including the URL of the record and the reason for the withdrawal request.

White Rose
university consortium
Universities of Leeds, Sheffield & York

eprints@whiterose.ac.uk
https://eprints.whiterose.ac.uk/

A branched magma feeder system during the 1669 eruption of Mt. Etna: evidence from a time-integrated study of zoned olivine phenocryst populations

Maren Kahl[1, 2, 3*], Marco Viccaro[4, 5], Teresa Ubide[6, 7], Daniel J. Morgan[3], & Donald B. Dingwell[2]

[1] Institute of Earth Sciences, University of Iceland, Sturlugata 7, IS-101 Reykjavík, Iceland

[2] Department of Earth & Environmental Sciences, LMU Munich, Theresienstrasse 41, 80333 München, Germany

[3] School of Earth & Environment, University of Leeds, LS2 9JT Leeds, United Kingdom

[4] Università di Catania, Dipartimento di Scienze Biologiche Geologiche e Ambientali - Sezione di Scienze della Terra, Corso Italia 57, I-95129, Catania, Italy

[5] Istituto Nazionale di Geofisica e Vulcanologia, Osservatorio Etneo, Piazza Roma 2, I-95125 Catania, Italy

[6] Department of Geology, Trinity College Dublin, Dublin 2, Ireland

[7] School of Earth and Environmental Sciences, The University of Queensland, Brisbane, QLD 4072, Australia

*Corresponding author. Present address: Institute of Earth Sciences, University of Iceland, Sturlugata 7, IS-101 Reykjavík, Iceland. Telephone: +354 525 4481. E-mail: marenk@hi.is

ABSTRACT

The 1669 eruption of Mt Etna was one of the most voluminous and devastating of its flank eruptions in historical times. Despite a large body of relevant research, knowledge of the timing and duration of magma transfer and magma recharge through the internal plumbing system preceding and during the eruption is still limited. To address that lack of knowledge, we apply a three-way integrated method, linking Systems Analysis of crystals, a time-integrated study of zoned olivine populations, and a forward-modelling approach using thermodynamic calculations. Analysis of 202 olivine crystals erupted during the initial (pre-March 20, i.e. *SET1*) and the final (post-March 20; i.e. *SET2* and *MtRs*) stages of the eruption reveals the existence of three different

Magmatic Environments (MEs) in which the majority of the olivine cores [M_1 (=$Fo_{75\text{-}78}$)] and rims [i.e. M_5 (=$Fo_{51\text{-}59}$) and M_3 (=$Fo_{65\text{-}69}$)] formed.

Application of the *rhyolite-MELTS* software enabled us to constrain the key intensive variables associated with these MEs. We find that temperature, water content and oxidation state vary between these MEs. Application of diffusion modelling to the zoned olivine crystals enabled us to reconstruct the timing and chronology of melt and crystal transfer prior to and during the 1669 flank eruption. We find, that following the formation of the olivine cores [M_1 (=$Fo_{75\text{-}78}$)], the reservoir M_1 was intruded by batches of more evolved, degassed and possibly aphyric M_5-type magma, commencing 1.5 years prior to eruptive activity. This is the origin of the *SET1* olivine rims (i.e. $Fo_{51\text{-}59}$). In the months prior to eruption, timescale data show that recharge activity along the newly established pathway M_1-M_5 increased notably. Starting in November 1668, only a few weeks after the first intrusive episode into the M_1 reservoir, a second pulse of magma injections (M_3-type magma) occurred and a new pathway M_1-M_3 opened; this is how the *SET2* olivine rims (i.e. $Fo_{65\text{-}69}$) formed. For several weeks a bifurcated transport system with two dominant magma pathways developed along M_1-M_5 and M_1-M_3 dyke injections. Accompanied by vigorous seismicity, in the immediate days prior to eruption the local magma transfer dynamics changed and the M_1-M_5 recharge activity slowed down, as shown by a relative lack of crystals recording shorter timescales. M_1-M_3 recharge, however, remained high and persisted following the eruption onset on March 11, during which the *SET1* lavas were drained. We propose that the change of the local magma transfer dynamics might be linked to changes in the local stress field brought on during eruption. This may potentially have been due to repeated dyke injections into Etna's shallow plumbing system disrupting the early M_1-M_5 pathway and at the same time stabilizing the M_1-M_3 route as a dominant feeder. This transfer of system feeding would reproduce the observed syn-eruptive recharge and mixing in the weeks following eruption onset, culminating in the eruption of the later *SET2* lavas.

KEYWORDS:

Olivine zoning; Plumbing system; Mt. Etna; Timescales; Magma mixing

INTRODUCTION

Geological setting

Mount Etna is a 3340-m-high (asl), composite stratovolcano located on the eastern coast of Sicily (Fig. 1) and covering a basal area of ~1250 km^2. It is located at the intersection of three tectonic domains, bounded by the transform Malta escarpment to the east, the Hyblean Plateau to the south and the subduction-related Aeolian arc to the north. To the west, subduction is blocked by compressive continental collision between the European and the African plate. Numerous models, including the southward migration of the Ionian slab (e.g. Schiano *et al.,* 2001) and the opening of a slab window (Gvirtzman & Nur, 1999; Doglioni *et al.,* 2001) have been proposed to explain the anomalous location of the volcano close to the suture zone of the African and European plates and its high magmatic flux. Geologically, the volcano rests on the southern edge of the over-thrust units of the Apennine-Maghrebian chain to the south (Fig. 1), and the undeformed remnants of the African margin to the southeast (e.g. Branca *et al.,* 2011). Volcanism is constrained to have started in the Etna region about ~500 ka ago (Gillot *et al.,* 1994; Branca *et al.,* 2011).

Types of eruptions at Mt. Etna: summit vs. flank activity

Like other basaltic stratovolcanoes, Etna is characterized by summit and flank eruptions. Summit eruptions are usually constrained to one of six central craters (Voragine, Bocca Nuova 1, Bocca

Nuova 2, Northeast Crater, Southeast Crater and New Southeast Crater) and the sub-terminal area (e.g. Corsaro *et al.*, 2009; Allard *et al.*, 2006; Branca and Del Carlo, 2004). Flank eruptions usually affect the intermediate and lower flanks of the volcano and can produce lava flow fields of considerable extent (e.g. the 1991-93 flank eruption produced a compound lava flow field of $240\pm29\times10^6$ m^3, Calvari *et al.*, 1994; Stevens *et al.*, 1997). Two different types of flank eruptions have been defined: 1. Central-lateral (Rittmann, 1965) or Central Conduit-Fed (CCF; Corsaro *et al.*, 2009) and 2. Eccentric (Rittmann, 1965), peripheral (Acocella and Neri, 2003) or Deep Dyke-Fed (DDF; Corsaro *et al.*, 2009) eruptions. Central-lateral flank eruptions originate by fracturing and lateral draining of the central conduits with the formation of eruptive vents at high altitudes. The eruption products resemble closely those erupted from the summit craters in being highly porphyritic (~30-40 % crystals) and plagioclase-rich due to significant water degassing in the central conduit system (e.g. Métrich *et al.*, 2004). Eccentric or deep dyke-fed (DDF) flank eruptions occur rarely [1763 (Corsaro *et al.*, 2009), 1974 (Corsaro *et al.*, 2009), 2001 (Lanzafame *et al.*, 2003; Behncke and Neri, 2003; Métrich *et al.*, 2004; Corsaro *et al.*, 2007; Ferlito et al., 2012) and 2002-03 (Andronico *et al.*, 2005; Spilliaert *et al.*, 2006)]. Eccentric eruptions are highly explosive with high tephra/lava ratios (e.g. Andronico *et al.*, 2005), and have low to medium phenocryst contents (<20% Andronico *et al.*, 2005), with dominantly mafic mineral phases (Armienti *et al.*, 1988; Corsaro *et al.*, 2009; Ferlito et al., 2012). As these eruption products differ from those of summit and central conduit-fed (CCF) flank eruptions, previous studies concluded that eccentric eruptions must have been driven by rapid ascent of deeply rooted intrusions - below the volcanic pile - that bypassed the shallow, central conduit system and therefore are undegassed (e.g. Corsaro *et al.*, 2009; Ferlito et al., 2012). Hence, this type of flank eruptions is also referred to as Deep Dyke-Fed (DDF; Corsaro *et al.,* 2009), as opposed to the more common central-lateral or Central Conduit-Fed (CCF; Corsaro *et al.*, 2009) flank eruptions.

The 1669 eruption: Characteristics and historical context

In this paper, we focus on the 1669 eruption, which is a central-lateral or Central Conduit-Fed flank eruption. The 1669 eruption was ranked as one of the most destructive and voluminous ($607 \pm 105 \times 10^6 m^3$, Branca *et al.,* 2013) flank eruptions of Mt. Etna in historical times (e.g. Corsaro *et al.,* 1996; Branca *et al.,* 2013). Between 1607 and 1669, 8 flank eruptions occurred on different sectors of the volcano; a brief summary of the duration, location of eruption vents and erupted volume is provided in Table 1. Preceded by a period of summit eruptions between 1654-1656 *(http://www.ct.ingv.it/en/11-notizie/news/561-etna-eruptions-pre1900.html)* and more than two weeks of increasing seismic activity (e.g. Corsaro *et al.,* 1996 and references therein), the 1669 eruption commenced in the early morning of March 11 through a system of NNW-SSE trending eruptive fissures that opened between 950 and 700 m a.s.l. (indicated as *1* in Fig. 1; Branca *et al.,* 2013). This first segment of the eruptive fracture system was characterized by weak and short-lived explosive activity. A second segment (*2*) opened shortly afterwards between 850 and 825 m a.s.l. and built a spatter rampart (Fig. 1). That same day (March 11) a third segment (*3*) opened between 850 and 775 m a.s.l. This became the main vent - Mt. Rossi - of the eruption (Fig. 1) and initially produced extended, explosive activity with ash fall followed by lava emission. The fourth segment (*4*) formed between 750 and 700 m a.s.l. close to the cone of Mt. Mompilieri (Fig. 1; Branca *et al.,* 2013); it was characterized by mild explosive activity and a minor lava flow. On March 12 a fifth segment (*5*) formed at the eastern base of Mt. Mompilieri between 700 and 640 m a.s.l. (Branca *et al.,* 2013). The eruptive activity continued for 122 days and destroyed several towns and settlements along the S-flank of Etna volcano until it ceased on July 11, 1669. Activity at the summit craters remained quiet during the flank eruption until March 25, when a violent explosive event occurred followed by the partial collapse of the summit cone (Corsaro *et al.,* 1996; Nicotra and Viccaro, 2012). A detailed report of the sequence of events and the evolution of the lava flow field during the 4 months of eruptive activity can be found in Branca *et al.* (2013).

In comparison to some of the historic and recent flank eruptions (e.g. 1991-1993), the 1669 eruption was relatively short-lived, with only four months of eruptive activity. During this brief interval of persistent eruptive activity, a compound lava flow field covered a total area of ~40 $\times 10^6$ m^2, with a total length of 17 km (Branca *et al.,* 2013). The relatively low altitude (800-850 m a.s.l.) of the erupting vents and high effusion rates (58±10 m^3/s, Branca *et al.,* 2013) enabled the lava flows to run over long distances. As a result, settlements located on the lower southern flank of the volcano, including the western districts of Catania were destroyed (e.g. Branca *et al.,* 2013). The 1669 flank eruption marks a major transition in terms of eruption intensity and petrography amongst the historic lavas (Corsaro *et al.,* 1996; Condomines *et al.,* 1995; Hughes *et al.,* 1990; Clocchiatti *et al.,* 1988; Guest and Duncan, 1981; Tanguy, 1980). Pre-1669 eruptions (1600-1669) were long-lasting, porphyritic and plagioclase-rich with high mean effusion rates (1.19 m^3/s; e.g. Hughes *et al.*, 1990; Branca *et al.,* 2013; Nicotra and Viccaro, 2012). In contrast, the post-1669 eruptions (1670-1755) were more sporadic and short-lived and had low output rates (0.02 m^3/s; Branca *et al.,* 2013). Post-1669 eruption products also contain predominantly mafic phase assemblages (Corsaro *et al.,* 1996).

It is possible that the steady increase in effusion rates during the first half of the 17th century culminated in the devastating March-July 1669 flank eruption. It has been argued that lateral draining of the central conduit system during the eruption caused not only the partial collapse of the summit cone (e.g. Corsaro *et al.,* 1996) but also had long lasting consequences for the evolution of Etna's shallow plumbing system (e.g. Condomines *et al.,* 1995). The impact of Etna's modified shallow plumbing configuration could be observed in the century following the

1669 eruption, with the 1670-1755 period displaying significantly lowered output rates (0.02 m^3/s; Branca *et al.,* 2013) and sparse flank activity (only 3 flank eruptions). It was only afterwards, in the period 1755 to 1970, that the mean effusion rate increased steadily up to 0.51 m^3/s (e.g. Branca *et al.,* 2013 and references therein).

Detailed geochemical and petrological studies of products of the 1669 eruption (Corsaro *et al.*, 1996) revealed that the erupted lavas are porphyritic hawaiites containing variable amounts of phenocrysts (porphyritic index; PI = 37-52 vol% phenocrysts) and mafic mineral phases (mafic mineral phenocrysts/total phenocrysts; CI_{Phx} = 10-53 vol%). Corsaro *et al.* (1996) found that the lavas erupted during the initial stages of the 1669 eruption (i.e. between March 11 and 20) differ considerably in their petrography (i.e. average PI=33 and CI_{Phx}=36 vol%) from lavas erupted after March 20 (average PI=44 and CI_{Phx}=18 vol%). Petrographic differences are also reflected in the major and trace element bulk geochemistry (Barbieri *et al.*, 1993; Corsaro *et al.,* 1996). Consequently, Corsaro *et al.* (1996) classified the 1669 lavas into two groups: *SET1* and *SET2*.

SET1 products were emplaced during the initial phase of the eruption, from March 11 to March 20, 1669. These samples have been described as being more 'basic' and 'magnesian', with similarities to later 18th and 20th century eruption products. *SET1* bulk rock compositions from Corsaro *et al.* (1996) are characterized by higher MgO (mean 6.65 ± 0.38 wt%) contents and higher compatible (i.e. Cr, Ni, Co, Sc) and incompatible (e.g. Th, La) trace element concentrations than the later erupted *SET2* lavas (Corsaro *et al.,* 1996). The *SET2* samples were emplaced after March 20, 1669 and are described by Corsaro *et al.* (1996) as plagioclase-phyric and more evolved in composition (e.g. mean MgO 5.07 ± 0.19 wt%) than the *SET1* eruption products. *SET2* lavas strongly resemble the plagioclase-phyric rocks of the early 17th century (Corsaro *et al.*, 1996).

Both sets of eruption products (*SET1* and *SET2*) were interpreted by Corsaro *et al.* (1996) as the result of fractional crystallization of two, compositionally-distinct primary magmas under distinct storage conditions, which fractionated different volumetric proportions of phenocrysts. Segregation was explained by the authors utilizing a 'laminar plume model', where mafic, gas-rich and therefore buoyant *SET1* magma rises through a pre-existing reservoir filled with *SET2* melt, without significantly (physically or chemically) interacting with it; this enables uprising *SET1* magma to retain its chemical and petrological signature, as mixing with *SET2* melt is inhibited.

The possibility of fresh magma inputs being able to bypass resident, more viscous magma is not new; such a model was invoked by Landi *et al.* (2006) to explain the segregation of volatile-poor degassed magmas and volatile-rich 'golden pumices' during the April 5, 2003 paroxysm of Stromboli volcano. In this case, bubble-driven ascent of deep volatile-rich magma through shallower resident magma enabled rapid ascent to the vent, with subsequent mixing only after the paroxysm. Despite a possibly shared characteristic of magma injections not mixing in the first instance, the Stromboli and Etna systems are quite different. A worrying implication of bypass behaviour is that intrusion and eruption can occur nearly simultaneously, and do not require a significant residence time of mafic magma in an evolved reservoir. This has considerable implications for the assessment of hazards posed by future 1669-type events, as it implies that similar, voluminous, low-elevation eruptions could commence with little warning. In fact, contemporary records indicate that signals of volcanic unrest in the form of vigorous seismic events, with epicenters located close to the town of Nicolosi on the southern flank of the volcano, preceded the 1669 eruption by approximately two weeks (e.g. Mulas *et al.*, 2016 and references therein); seismic activity increased on March 08, 1669, culminating in the eruption onset on March 11, 1669 (Mulas *et al.*, 2016 and references therein; Tanguy and Patanè, 1996). The purpose of this paper is to obtain new insights into the plumbing system feeding the 1669 flank eruption and test viability (and hence hazard implications) of quick melt bypass.

Etna's *modern (1991-2008)* plumbing system: Insights from a crystal chemistry perspective

In previous studies, Kahl *et al.* (2011, 2013 & 2015) developed a novel petrological methodology linking a *Systems Analysis* approach to compositionally-zoned olivine populations with a time-integrated study (i.e. diffusion modelling in olivine). This approach was successfully applied to samples from recent summit and flank (i.e. 1991-2008) eruptions at Etna volcano to reconstruct the residence and migration history of magma through Etna's modern plumbing system (Kahl *et al.,* 2015). The present study uses and builds upon existing techniques and results developed by Kahl *et al.* (2011, 2013 & 2015). Therefore, in this section, we review some of the main methods and concepts and briefly summarize what we know so far about Etna's modern plumbing system from a combined crystal chemistry and kinetic modelling approach.

Studying the compositional and zoning record of 180 olivine crystals that were erupted between 1991 and 2008 at Mt. Etna, Kahl *et al.* (2011, 2013 and 2015) recognized that zoning profiles of Fe-Mg and selected trace elements (e.g. Ni, Mn, Ca) in olivine contain core and/or rim compositional plateaux with diffuse boundaries separating them. The occurrence of such compositional plateaux was interpreted as sequential growth of olivine under a constant set of intensive thermodynamic variables (pressure, temperature, composition, fugacities of volatile species) defining a certain Magmatic Environment (ME). This is opposed to progressive changes, such as cooling or differentiation that would result in continuous variations of composition rather than plateaux separated by sudden jumps or diffuse boundaries (Kahl *et al.,* 2015). A Magmatic Environment (ME) may represent a physically distinct entity (e.g. a sill, dyke), or a virtual entity (e.g. a set of P, T, X, fO_2, fH_2O conditions within a zoned larger magma reservoir). Kahl *et al.* (2011, 2013 and 2015) used the terms "magmatic reservoir" and "magmatic environment" to distinguish the physical entity from the virtual entity defined by a set of intensive variables; the two may be the same (e.g. in an unzoned magma reservoir of small enough size) but do not have to be. Kahl *et al.* (2011) assumed that the compositional variation from core to rim in a crystal represents a chemical stratigraphy and that the compositional record can be used to identify and effectively track different MEs crystals passed through on the way to eruption. Consequently, the change in zoning pattern from one plateau to another is equivalent to the transfer of the crystal from one ME to another. This can be accomplished either by the crystal physically moving (with some melt) from one environment to another, or by the environment itself changing around the crystal (e.g. by cooling or degassing). To be able to track effectively the sequence of magmatic events preserved in the chemical stratigraphy of populations of zoned olivine crystals, Kahl *et al.* (2011) developed the tool of *Systems Analysis*. This allows to decipher the record of different pathways (sequences of changes in MEs) stored in the crystal cargo of a given rock by using connectivity diagrams to organize the compositional information. The frequency of connections found in the connectivity diagrams (diagrams where successive compositional plateaux are connected by directed line segments; the direction pointing from core toward rim) are taken to provide a measure of the relative frequency with which pathways between different environments were used. For example, Kahl *et al.* (2011) discovered that a single thin section of a lava flow from the 1991-93 SE flank eruption of Etna, contained olivine phenocrysts with three different types of zoning patterns (normal, reverse and complex) and compositions ranging from Fo_{83} to Fo_{70}. Compositional plateaux in the olivine crystals were consistent with four MEs that, when considered with the relevant diffusive modifications, could be used to describe the total diversity of compositional variation in the olivine phenocrysts that were erupted between December 1991 and March 1992 (Kahl *et al.,* 2011). The width of the diffusion zone between two compositional plateaux and the shape of the concentration profiles record the duration and residence time a crystal spent within a given ME. Hence, Kahl *et al.* (2011) developed the tool of *sequential kinetic modelling* that allows working backward - from the rim to the core - the durations a crystal spent in different MEs prior to eruption. Finally, Kahl *et al.* (2015) developed a forward modelling approach using thermodynamic calculations with the MELTS software (Ghiorso and Sack, 1995; Asimow and Ghiorso, 1998) to identify the key intensive variables associated with the different Magmatic Environments identified. In this approach the observed populations of mineral compositions (e.g. $Fo_{79–83}$) defining a certain ME (e.g. M_0), rather than single compositions, are associated with thermodynamic parameters (P, T, water content, oxygen fugacity and bulk composition of melt) to identify the most plausible set corresponding to each ME.

Application of this combined and novel methodology that links the crystal chemistry with a time-integrated study and forward thermodynamic modelling enabled Kahl *et al.* (2011, 2013 and 2015) to investigate the temporal evolution of Etna's modern plumbing system across multiple eruptive episodes of different styles, and at different locations. Considering the comprehensive compositional and zoning record preserved in 180 olivine crystals that erupted between 1991 and 2008, five MEs were identified: M_0 ($Fo_{79–83}$), M_1 ($Fo_{75–78}$), M_2 ($Fo_{70–72}$), M_3 ($Fo_{65–69}$) and mm_1 ($Fo_{73–75}$). Kahl *et al.* (2015) found that the same MEs as those deduced by Kahl *et al.* (2011, 2013) to describe the observed variability of olivine compositions erupted during the 1991-93 flank and the 2006 summit eruptions, could be used to describe the compositional variations recorded in all 1991-2008 olivine crystals. The combined Systems Analysis record of all eruption products revealed that although the MEs remained the same during 17 years, the interconnectivity between them and hence the dominant magma pathways changed with time. Main changes were found either between large eruptions (1991-93 and 2001) or between eruptive episodes.

For example, Kahl *et al.* (2013) studied the compositional and zoning record of olivines that were erupted during two different events (July 20 and October 28) of the 2006 summit eruptions at Mt. Etna. The authors discovered that olivines of the July 20 and the October 28, 2006 eruptions were not only characterized by different zoning patterns but also by different core and rim plateau compositions. The July 20 olivines were reversely zoned with low forsterite core (=Fo_{70-72}) plateaux and higher forsterite rims (=Fo_{73-75}). 3 months later, during the October 28 event, olivines showed dominantly normal zoning with high forsterite core plateaux (=Fo_{79-82}) and decreasing forsterite contents at the rims (=Fo_{70-72}). Based on the different core and rim plateau compositions and the different zoning types (normal vs. reverse) three different MEs [M_0 (=Fo_{79-82}), M_2 (=Fo_{70-72}) and mm_1 (=Fo_{73-75})] with diverging connectivity patterns were observed. Olivines erupted in July showed a dominant population of crystals connecting the environments M_2-mm_1, whereas olivines erupted in October tracked a different history between M_0-M_2. Kahl *et al.* (2013) argued that these different connectivity patterns revealed by the *Systems Analysis* of the 2006 olivine zoning and compositional record may be attributed to a small but significant change in the magma transport regime in the course of the 2006 eruption. They also concluded that such a change - that occurred only within months - may be explained best by a short-term change of the plumbing system sometime between July and October 2006. This agreed well with the observation that the July and October 2006 events occurred from different eruption centres.

By means of the Systems Analysis approach, Kahl *et al.* (2015) found that three dominant magma transfer routes connecting the environments M_0-M_1, M_2-mm_1 and M_1 -M_2 have been active during the entire period (1991-2008). These MEs therefore represent robust and long-term features of Mt. Etna's plumbing system that may have facilitated the transfer of magma to the surface for nearly two decades. In parallel, they also identified some sparsely frequented routes connected to more evolved MEs such as M_3 ($Fo_{65–69}$). Migration routes connected to this environment could be identified only in some eruption products and were therefore inferred to represent temporary pathways of magma transfer that were activated only occasionally or were traversed too quickly to be recorded in all olivine zoning profiles. The significance of such highly evolved but rarely tapped environments and their role in Etna's historic plumbing system will be evaluated further in this study. An important observation of Kahl *et al.* (2011, 2013 and 2015) is the discovery of pre- and/or syn-eruptive pulses of mafic magma recharge into different MEs of the plumbing system, indicated by olivine populations with forsterite M_0 ($Fo_{79–82}$) core and/or rim compositions.

The application of sequential kinetic modelling revealed that the transfer of magma along the three most dominant routes in Etna's modern plumbing system M_0-M_1, M_2-mm_1 and M_1-M_2 occurred over heterogeneous timescales ranging from days to 2 years. Although some of the passageways have been sporadically active in the months and sometimes years before an eruption, the magma migration activity increased in the weeks and days prior to an eruptive event. For example, recharge of the environments M_1 and M_2 began years before an eruption, but became more frequent in the last few days prior to its onset (Kahl *et al.*, 2015). On the other hand, other environments such as mm_1 were found to represent transient features of Etna's modern plumbing system and formed within the last 40 days before eruptive activity commenced (Kahl *et al.*, 2015).

Kahl *et al.* (2015) conclude that temperature, water content and possibly oxidation state are the main distinguishing features of the different magmatic environments. They found that: M_0 ($Fo_{79–}$

$_{83}$), the most primitive olivine population may have grown with some clinopyroxene at high water contents (3.5–5.2wt %) and fO_2 conditions buffered at QFM or NNO at pressures ranging between 1.5 and 3.0kbar (or even higher). Temperatures of >1110˚C are required. The intermediate olivine population M_1 ($Fo_{75–78}$) could have formed over a broad spectrum of conditions, but all require lower water contents (0.1–1.4wt %) at similar temperatures. The most evolved, Fe-rich olivines of M_2 and M_3 (Fo_{70-72} and Fo_{65-69}) are the products of extremely dehydrated magmas (0.2–1.1wt % H_2O for M_2; <0.5wt % H_2O for M_3), and probably somewhat more reducing (QFM) conditions that were most probably obtained at even shallower depths and at somewhat lower temperatures (~1080˚C).

The findings of multi-level magma transfer between different MEs within Etna's modern plumbing system derived by Kahl *et al.* (2011, 2013 and 2015) agrees with evidence from geophysical (e.g. Aloisi *et al.,* 2002; Lundgren *et al.*, 2003; Murru *et al.*, 1999; Bonaccorso *et al.*, 2011; Patanè *et al.*, 2003, 2006 and 2013; Viccaro *et al.*, 2016a) and thermobarometric (e.g. Armienti *et al.*, 2013; Giacomoni *et al.*, 2014 and 2016) studies. Thermobarometry calculations indicate that clinopyroxene starts crystallising at depth >20km (e.g. Armienti *et al.*, 2013; Giacomoni *et al.*, 2016) and continues until eruption. The deep to intermediate crystallisation range of clinopyroxene coincides with the detection of deep VT seismicity in the intermediate and lower crust (10-30km, Patanè *et al.*, 2013) interpreted as periodic ascent of magma batches from the mantle (Patanè *et al.*, 2013). Plagioclase was found to start crystallising at shallower depths in the upper crust (>12km depths), with the majority nucleating around 5-6km and continue (like clinopyroxene) to crystallise until eruption (Viccaro *et al.,* 2010 and 2016b; Giacomoni *et al.*, 2014 and 2016). These crystallisation levels coincide with the detection of low-velocity zones using seismic tomography (e.g. Murru *et al.,* 1999). The crystallization of both, plagioclase and clinopyroxene seems to be continuous in a polybaric vertical feeding system, in which at least two different magma crystallisation levels have been identified (Armienti *et al.*, 2013; Giacomoni *et al.*, 2014 and 2016).

This study

Here we apply the combined methodology developed by Kahl *et al.* (2011, 2013 and 2015) to the 1669 eruption products, and investigate olivine zoning using novel imaging of crystallographic orientation and trace element distribution. Our aim is to (i) test the existence and duration of pre- and syn-eruptive mixing of *SET1* and *SET2* magmas, (ii) obtain the residence times of *SET1* and *SET2* magmas within the plumbing system prior to eruption and (iii) reconstruct the pre- and syn-eruptive history of magmatic events leading to the 1669 flank eruption.

We first present a brief chronology of the eruption sequence, followed by descriptions of the relevant aspects of petrography and mineral chemistry, the types of zoning found in olivine and their major, minor and trace element compositional characteristics. We use these data to construct connectivity diagrams and carry out Systems Analysis, in order to determine the nature of magma transfer throughout the plumbing system. Then we undertake a forward-modelling approach of thermodynamic calculations using the *rhyolite-MELTS* software (Gualda *et al.,* 2012; Ghiorso & Gualda, 2015) to constrain the physical conditions of the identified Magmatic Environments (MEs). Subsequently, we perform diffusion modelling to determine the timing and duration of magma mixing and magma migration between the different MEs. Finally, we synthesize our findings and results to develop a conceptual model of the late stage magmatic history before and during the 1669 eruption.

SAMPLES

A total of 10 lava samples and 1 bomb sample were studied, representing different episodes of the 1669 flank eruption. The locations of all samples studied are highlighted in Figure 1 and the sampling locations and GPS coordinates are listed in Table 2. We collected 5 lava samples from a flow unit that was emplaced on March 19, 1669. These samples erupted before March 29 and therefore belong to the *SET1* lavas as defined by Corsaro *et al.* (1996) (Fig. 1). Another 5 samples were collected from a lava flow that reached the outskirts of Catania (Fig. 1). This flow was emplaced after March 29 (possibly on April 4, 1669) and therefore falls into the *SET2* lavas of Corsaro *et al.* (1996). The bomb sample was collected at the top of the Mt. Rossi (*MtRs*) scoria cone (Fig. 1). An exact eruption date for this sample is not available, but given its location at the top of the cone that fed most of the eruption, we infer that it erupted towards the end of the volcanic activity and therefore belongs also to the *SET2* category (erupted after March 20, 1669; Corsaro *et al.*, 1996).

ANALYTICAL METHODS

X-ray fluorescence (XRF)

Whole rock compositions were determined by WD-XRF analysis (*MagiX PRO XRF, Philips*) at the Department for Earth & Environmental Sciences (DEES) at LMU. Major and minor elements were analyzed using glass beads prepared by fusion of 1 g sample and 9 g *SPECTROMELT A12* (66 % di-lithium tetraborate, 34 % lithium metaborate) in a *Panalytical Eagon 2* furnace fusion system at 1150°C. Analytical precision was checked against a basalt standard and reproducibility was found to be better than 0.15%.

Electron microprobe (EMP)

Olivine

Backscattered electron (BSE) images and detailed, quantitative concentration profiles (spacing ~4-5µm) of major and minor elements (Si, Fe, Mg, Mn, Ca, Ni and Cr) along different directions in a total of 202 olivine crystals were obtained using a Cameca SX-100 electron microprobe (EMP) at the Ludwig-Maximilians Universitaet (LMU) Muenchen. Run conditions were: 15kV accelerating voltage, 20-30nA beam current and a focused electron beam (1µm) for the analysis of olivine. Peak and background counting times of 10s were used for each element. Well-characterized synthetic oxides and minerals were used as analytical standards including (Si, Mg) olivine, (Ca) wollastonite, (Fe) almandine and andradite, (Mn) $MnTiO_3$, (Cr) Cr_2O_3 and (Ni) NiO.

Clinopyroxene

Major and minor element concentrations (Si, Fe, Mg, Mn, Ca, Ni, Na, Al, Ti, Cr and K) of 62 olivine–clinopyroxene pairs and single clinopyroxene crystals (spacing 3–6µm) were obtained using a Cameca SX-100 electron microprobe (EMP) at the Ludwig-Maximilians Universitaet (LMU) Muenchen. A total of 829 single spot analyses were made at 15kV and 30nA, using a focused beam (1 µm). The counting times at peak and background for each element were set to 10–20s.

Fe–Ti oxides

74 single-point analyses across the contact zone between adjacent olivine and Ti-magnetite were made (Si, Fe, Mg, Mn, Ca, Ni, Na, Al, Ti, Cr and K) using a Cameca SX-100 at the Ludwig-Maximilians Universitaet (LMU) Muenchen. Run conditions were the same as for olivine.

Analytical quality was ensured by analysing the reference materials as unknowns and by mineral stoichiometry calculations (Deer *et al.* 2013).

Electron backscatter diffraction (EBSD)

Crystallographic orientations of olivine crystals were determined using electron backscatter diffraction (EBSD, Prior *et al.,* 1999; Costa & Chakraborty, 2004) on the FEI Quanta 650 FEGSEM at the University of Leeds Electron Microscopy and Spectroscopy Centre (LEMAS). Constraint of crystallographic directions in olivine with respect to the micro-analytical traverses is essential for accurate diffusion modelling, as the diffusivity of different elements (e.g. Fe-Mg or Ni) in olivine is strongly anisotropic, with diffusion along the c-axis six times faster than along the a- and b-axes (e.g. Dohmen *et al.,* 2007a; Clark & Long, 1971).

To minimize uncertainty in the determination of the orientation data, orientation maps (Fig. 2c, d) consisting of hundreds of EBSD point determinations were conducted for each grain. Using the *HKL CHANNEL5* EBSD post-processing software, orientation-maps are generated over an entire crystal, extracting hundreds to thousands of individual orientation measurements. This comprehensive approach is enabled by rapid acquisition, and improves on earlier methods in which only a few points per olivine grain were measured. Due to the improved coverage and resolution, features such as internal lattice misorientations, sub-grain boundaries, twins and pseudo-symmetries can be easily identified. EBSD mapping of this type is novel and has not been routinely used by the diffusion community so far. Operating conditions are available as Supplementary Data (SD) Electronic Appendix 1 (supplementary data are available for downloading at http://www.petrology.oxford journals.org).

Laser Ablation Inductively Coupled Plasma Mass Spectrometry (LA-ICP-MS) mapping

The elemental distribution of 7 olivine crystals was determined by LA-ICP-MS mapping at the Geochemistry Laboratories of Trinity College Dublin, according to the method developed in

Ubide *et al.* (2015). The analyses were made on typical 30 μm-thick polished sections of rocks from *SET1*, *SET2* and the *MtRs* samples.

LA-ICP-MS mapping experiments were carried out using a Photon Machines G2 193 nm excimer Ar-F laser system with a Helex 2-volume ablation cell, coupled to a quadrupole Thermo iCapQc mass spectrometer. The carrier gas was a mixture of He and Ar (and minor N_2 introduced via an in-house developed variable volume smoothing device). The laser was operated with a fluence of 2.5 J/cm^2. The mapping area was built by overlapping individual ablation lines to form a rectangular grid. The laser spot size was determined by the size of olivine crystals and set at 10 μm. Ablation lines were built using a square laser mask, 15 μm/s scanning speed, 10 Hz repetition rate and 1 μm overlap between lines, following Ubide *et al.* (2015). A baseline measurement of 30 to 40 s was allowed between ablation lines. Given the typical bright colour of olivine grains in thin section, it was found that pre-ablation of the crystals using large, quick rasters (e.g., 85 μm circle laser beam, 160 μm/s scan speed, 20 Hz repetition rate, 1 μm overlap between lines) improved the ablation of olivine in the subsequent mapping experiment, producing sharper element maps. The analytes were ^{25}Mg, ^{27}Al, ^{29}Si, ^{31}P, ^{43}Ca, ^{45}Sc, ^{49}Ti, ^{51}V, ^{52}Cr, ^{55}Mn, ^{57}Fe and ^{60}Ni. Seven to ten analytes were measured in each individual mapping experiment, with a total dwell cycle of 100 to 110 ms.

NIST612 glass reference material (Jochum *et al.,* 2011) was used at the beginning of each analytical session to tune the instrument. NIST610 glass reference material (Jochum *et al.,* 2011) was used as calibration standard for all mapping experiments. Data reduction and production of element distribution maps was undertaken with Iolite v2.5 free software (Paton *et al.,* 2011) using the 'Trace_Elements_Image' data reduction scheme (Ubide *et al.,* 2015). Following Chew *et al.*

(2016), maps were initially built in ‘Semi quantitative’ mode and the scales were subsequently normalized to the Si content measured independently (38.5 wt.% SiO_2 from olivine EMP data).

PETROLOGY

The 1669 eruption products are strongly porphyritic. The rocks contain the typical Etnean phenocryst assemblage of plagioclase (~12-15 vol.%), clinopyroxene (~8-11 vol.%), olivine (~3–5 vol.%), and accessory Fe–Ti oxides (~<3 vol.%) embedded in a fine-grained, hypo-crystalline groundmass. The groundmass consists of micro-laths of plagioclase, Fe–Ti oxides, clinopyroxene and variable amounts of interstitial glass. The abundances and relative proportions of phenocrysts (porphyritic index PI) can vary significantly (PI ranging between 37 and 52%) between individual eruption products (cf. Corsaro *et al.,* 1996).

Plagioclase ($An_{56–85}$) forms mostly euhedral phenocrysts of variable size (0.2 - 4 mm). Plagioclase phenocrysts contain multiple sequences of oscillatory zoning as well as strong dissolution (sieve) textures (see also Corsaro *et al.,* 1996).

Clinopyroxene ($Wo_{46–48}$, $En_{36–41}$, $Fs_{13–16}$ and Mg#73-93; see SD Electronic Appendix 2) forms euhedral to subhedral phenocrysts with sizes ranging between 0.8 and 4.8 mm. Pronounced sector and oscillatory zoning and inclusions of Fe–Ti oxides are common; rare inclusions of plagioclase and olivine are also found.

Olivine ($Fo_{51–83}$; see SD Electronic Appendix 3) is mostly subhedral or anhedral with slight dissolution features (e.g. rounded edges) and core–rim zonation. The size of olivine phenocrysts ranges between 0.2 and 1.5 mm.

Opaque Fe–Ti oxides ($Uvsp_{33-60}$, Spn_{13-26}, Mt_{35-53}; see SD Electronic Appendix 4) form euhedral to anhedral phenocrysts or occur as inclusions in clinopyroxene and olivine crystals and in melt embayments.

Whole rock compositions of *SET1* and *SET2* lava and the MtRs bomb sample (Table 3) are plotted in a TAS diagram in Fig. 3a. For comparison, bulk rock data of *SET1* and *SET2* samples analysed by Corsaro *et al.* (1996) and Mulas *et al.* (2016) were added. The 1669 volcanic products are hawaiitic in composition. We observe that there is a compositional offset between our samples and some of the samples analysed by Corsaro *et al.* (1996). Mulas *et al.* (2016) have also reported a similar offset. Our *SET1* and *SET2* samples are relatively similar in composition to *SET1* samples from Corsaro et al. (1996) and to the pyroclast samples studied by Mulas *et al.* (2016). By contrast, *SET2* lavas from Corsaro *et al.* (1996) have higher SiO_2, Al_2O_3 and total alkalis (Fig. 3a, 3b, 3c) and lower TiO_2 and FeO contents (Fig. 3d-e). Our *SET1* and *SET2* samples have similar MgO contents (Fig. 3h-l) to the *SET2* samples of Corsaro *et al.* (1996). According to the petrological descriptions in Corsaro *et al.* (1996), their *SET2* samples contain abundant plagioclase phenocrysts and as a result, a generally lower phenocryst colour index (CI_{phx} = mafic mineral phenocrysts/total phenocrysts, vol.%; CI_{phx}=18) than their *SET1* samples (CI_{phx}=36; see their Fig. 2). Such plagioclase-rich rocks are common at Mt. Etna and, when characterized by megacrystic plagioclase, are locally known as cicirara (see also Nicotra & Viccaro, 2012). Given that recent studies on porphyritic mafic systems have highlighted that accumulation of early mineral phases plays a major role on whole rock compositional variations (e.g. Sakyi *et al.,* 2012; Larrea *et al.,* 2013; Ubide *et al.,* 2012, 2014), such variations need to be evaluated in terms of differential accumulation of phenocryst phases.

To investigate this possibility, we present selected variation diagrams of bulk rock data together with representative phenocryst compositions as Supplementary Data (SD) in Electronic Appendix 5, following the approach of Ubide *et al.* (2014). The anomalous composition of *SET2* samples from Corsaro *et al.* (1996) (i.e., higher concentrations in SiO_2, Al_2O_3 and total alkalis and lower concentrations in FeO and TiO_2 than the other bulk rock samples; Fig. 3) would agree with preferential accumulation of plagioclase phenocrysts over olivine/clinopyroxene phenocrysts. In addition, we find that our samples have higher contents of CaO (mean 10.51 wt% *SET1* and 10.36 wt% *SET2*) and lower concentrations of MgO (mean 5.15 wt% *SET1* and 5.02 wt% *SET2*) than the *SET1* samples (Fig. 3f, g) studied by Corsaro *et al.* (1996). This could be related to preferential accumulation of clinopyroxene over olivine in our samples. Therefore, we interpret that the small geochemical variations observed between bulk samples could be related to preferential accumulation of varied phenocryst phases. In other words, *SET1* and *SET2* lavas are likely composed of similar melts accumulating slightly varied phenocryst cargoes (SD Electronic Appendix 6).

OLIVINE ZONING & COMPOSITIONAL RECORD

Olivine zoning patterns

We studied a total of 202 olivine crystals (*n=117 SET1*; *n=68 SET2*; *n=17 MtRs*) across the 11 samples studied. 198 (98%) of the studied olivine crystals were characterized by systematic *normal* (decreasing forsterite contents towards the rims) and to a minor extent (2%, i.e. 4 crystals) also *reverse* (increasing forsterite contents towards the rims) zoning patterns. These are classified by zoning type into the same classification scheme employed by Kahl *et al.* (2015), who studied a total of 180 olivine crystals from recent (1991-2008) eruption products of Etna. The 1991-2008 olivines were characterized by multiple zoning patterns ranging from *normal* to *reverse*, or more *complex* zoning, with reversely zoned cores and normally zoned rims. Based on this large range of zoning patterns, Kahl *et al.* (2015) established 8 different zoning types (*Type I* – *Type VIII*). Extending that classification scheme to the 1669 olivines, we observe that the zoning patterns preserved in the 1669 olivines consist predominantly of simple *single-step* normal or reverse zonations. This finding contrasts with the diversity of olivine zoning patterns identified in the recent 1991-2008 eruption products. From the 8 zoning types (*Type I – Type VIII*) described in Kahl *et al.* (2015), 6 could be recognized in the 1669 olivines. Of those, *Types IV* and *VII* (Fig. 4) are the most abundant (186 crystals out of 202):

- *Type IV* represents normally-zoned crystals with intermediate core compositions of Fo75-78 followed by low forsterite rims (~Fo_{55} for *SET1*; ~ Fo_{70} for *SET2* and *MtRs*; Fig. 4a). This zoning type is by far the most abundant observed in the 1669 samples. It is identified in 71% (i.e. 144 crystals) of the studied olivines and can be found in all samples.

- *Type VII* describes normally zoned crystals (21%, i.e. 42 crystals) with cores at Fo73-75 and variable rim compositions (~Fo_{55} *SET1* and ~Fo_{70} *SET2*; Fig. 4b). Together with *type IV* this zoning type occurs frequently in the *SET1* and *SET2* olivines. In the *MtRs* bomb sample, *type VII* could not be identified.

Besides these two dominant groups, minor zoning types (16 out of 202 crystals) have been identified (see SD Electronic Appendix 7):

- *Type I*: Reversely zoned crystals with low forsterite (Fo_{70-72}) cores and rim compositions at Fo_{75}.

- *Type II:* Normally zoned olivines with high forsterite cores (Fo_{79-83}) and rims of variable composition (Fo_{70-71} for *SET2*).

- *Type VI:* Crystals consisting of weak reverse zoning with intermediate core compositions (Fo_{73-75}) followed by subtle increase of the forsterite content towards the rims (~Fo_{75}) and reverse zoning with decreasing forsterite values at the outermost rims (Fo_{72}). The occurrence of this zoning type is limited to the Monte Rossi bomb sample.

- *Type VIII:* Normally zoned crystals with low forsterite core composition at Fo_{70-72} and rim compositions as low as Fo_{55}. This type is limited to *SET1* eruption products.

Olivine compositional record

Besides variable zonation sense and pattern, the 1669 olivine crystals differ in terms of their specific core and rim compositions; the observed olivine compositions vary over a considerable range from Fo_{51} up to Fo_{83}. In Fig. 5a, b frequency histograms illustrate the distribution of core and rim compositions of the 202 olivine crystals studied. All olivine data are provided in SD Electronic Appendix 8.

The observed core compositions display a narrow compositional spectrum ranging from Fo71 to Fo83 with a dominant peak at Fo_{75} (Fig. 5a). The rim compositions, however, show a much broader compositional range from Fo_{51} up to Fo_{78} (Fig. 5b). Overlap between the *SET1* and *SET2-MtRs* does occur but is minor, affecting ~6 % of the crystals (i.e. 13 crystals), which have definably different compositional modes. We observe different modes in the rim compositional record of the *SET1*, *SET2* and *MtRs* olivines. *SET1* olivine rims display compositions ranging between Fo_{51} and Fo_{65}, whereas the *SET2* and *MtRs* rims vary between Fo_{64} and Fo_{77}, with a peak at Fo_{69} (Fig. 5b). This will be discussed in more detail in the following section.

In Figures 5c-h minor element (MnO and CaO) plots of olivine core and rim compositions are shown. The olivine cores and rims show a negative correlation between forsterite and MnO content (Fig. 5c, d). The MnO contents of the olivine cores range between ~0.3 wt% for Fo_{80-83} and 0.7 wt% for Fo_{71}. The rims have MnO contents ranging from 0.4 wt% for Fo_{75} (*SET2* and *MtRs* samples) up to ~1.35 wt% for Fo_{51} (*SET1* samples).

The CaO contents of the olivine cores and rims are less variable, and range between 0.2 and 0.4 wt% for the cores (Fig. 5e) and between 0.3 and ~0.6 wt% (Fig. 5f) for the rims. Combining the CaO and MnO data, we find that the *SET1* and *SET2-MtRs* olivines not only differ in their forsterite contents but also in their minor element chemistry (Fig. 5g, h), defining distinct fields. *SET1* olivine rims are characterized by higher MnO and CaO contents than *SET2* and *MtRs* rims. We take this as evidence that the olivine rims of *SET1* and *SET2* formed within compositionally different Magmatic Environments (MEs) that controlled both the major and minor element chemistries. By contrast, *SET1* and *SET2* olivine cores formed within the same ME.

Comparison with olivine compositions from recent (1991-2008) eruptions of Mt. Etna

For comparison, we have added in Figure 5 a-f the compositional range of the 5 different MEs identified in populations of zoned olivines erupted between 1991 and 2008 from Etna volcano (Kahl *et al.,* 2015).

We find that the core compositional record of the 1669 olivines plots within the range of known olivine compositions (i.e. Fo_{65-83}) from recent and historical Etna eruptions (e.g. Clocchiatti & Métrich, 1984; Tanguy & Clocchiatti 1984; Chester *et al.,* 1985; Métrich & Clocchiatti, 1989; Corsaro *et al.,* 1996; Spilliaert *et al.,* 2006; Corsaro *et al.,* 2009; Kahl *et al.,* 2015). The most dominant core population - that can be tracked throughout all 1669 eruption products - is Fo_{75-78} (144 crystals) followed by minor populations at Fo_{73-75} (45 crystals), Fo_{70-72} (10 crystals) and Fo_{79-83} (3 crystals). We observe that the two prominent olivine core populations in the 1669 products fall within the compositional range of the known Magmatic Environments (MEs) M_1 (=Fo_{75-78}) and mm_1 (=Fo_{73-75}; Fig. 5).

Regarding rim compositions, we observe two clearly distinct groups in the 1669 olivine dataset:

- *SET2 and MtRs:* The rim compositional record of the *SET2* and *MtRs* olivines displays two dominant populations at Fo_{65-69} (49 crystals) and Fo_{70-72} (30 crystals) and fall within the range of known Magmatic Environments M_3 (=Fo_{65-69}) and M_2 (=Fo_{70-72}) described in Kahl *et al.* (2015). Minor populations can be observed at Fo_{73-75} (4 crystals) and Fo_{75-78} (2 crystals) and resemble the MEs defined by the olivine cores [i.e. M_1 (=Fo_{75-78}) and mm_1 (=Fo_{73-75})].

- *SET1:* The *SET1* olivine rim compositions define a new compositional trend undetected in the recent eruption products. *SET1* rim compositions can be roughly subdivided into two populations, one at Fo_{60-65} (17 crystals) and a second, bimodal population between Fo_{51} and Fo_{59} (99 crystals) with subtle peaks at Fo_{54} and Fo_{57}, respectively (Fig. 5b). From the minor element plots we can observe that both populations clearly differ from others by higher MnO and CaO contents (Fig. 5d, f). We infer therefore that *SET1* olivine rims formed in a Magmatic Environment distinct from those seen in recent products, which we define here as M_5.

Olivine trace element mapping

LA-ICP-MS element maps were obtained for selected olivine crystals Ol-5 (*Type IV*), Ol-12 (*Type IV*) and Ol-21 (*Type IV*) from sample 1-6 (*SET1* lavas), Ol-1 (*Type IV*) and Ol-4 (*Type IV*) from sample 2-4 (*SET2* lavas), and Ol-4 (*Type IV*) and Ol-6 (*Type VI*) from the MtRs bomb. Representative maps for minor and trace elements are presented in Fig. 6.

Olivine crystals show homogeneous cores and normally-zoned rims. Concentrations in Mg and Ni decrease from the core to the rim of the crystals, and concentrations in Fe, Mn and Ca increase accordingly. Such compositional change is observed in all analysed crystals, supporting EMP results. In addition, LA-ICP-MS maps show that core-rim zoning is sharper in *SET1* olivines, which show thicker, better developed rims than *SET2-MtRs* olivines (Fig. 6). Concentrations in V, Cr, Al, P, Sc and Ti are largely homogeneous across all olivine crystals and no zoning has been detected for these elements.

In summary, the detailed investigation of major, minor and trace element zoning profiles in 202 olivines reveals the existence of distinct compositional zonation (typically normal zonation) throughout all eruption products studied (*SET1, SET2* and *MtRs*). This observation contrasts with the finding of Corsaro *et al.* (1996), in which the lack of compositional zoning in olivine phenocrysts (cores: $Fo_{73–77}$; rims: $Fo_{73–74}$) was reported suggesting a sub-solidus homogenization, due to diffusive relaxation. An interesting observation arising from this study that has not been reported so far is the compositional variability and difference between the *SET1* and *SET2-MtRs* olivine rims indicating that the olivine crystals (and their melts) experienced distinct and different late-stage magmatic histories following the formation of the cores. Although the *SET1* and *SET2* samples investigated in this study are rather similar in whole rock composition, we find that in-situ compositional information locked in the chemical stratigraphy of zoned olivine crystals reveals significant differences between the *SET1* and *SET2-MtRs* samples.

UNRAVELLING THE ZONING RECORD

As outlined in Kahl *et al.* (2011 & 2015) a characteristic that all identified olivine populations have in common, is the existence of so-called compositional plateaux: zones or regions within a crystal characterized by constant forsterite values (Fig. 4; SD Electronic Appendix 7). The occurrence of these plateaux was attributed to the stepwise growth of the crystals within different MEs, which in turn may be characterized by a different set of thermodynamic parameters (e.g. temperature, pressure, oxygen fugacity, water content and melt composition). In order to produce extended plateaux of constant forsterite contents the ambient parameters must have been kept constant during growth, otherwise continuous variations in the compositional profiles (as observed during cooling or fractionation) rather than plateaux with sudden jumps, would be expected (Kahl *et al.,* 2015).

We make use of the method outlined in Kahl *et al.* (2011) to illustrate the comprehensive zoning record preserved in the studied olivine crystals in Systems Analysis diagrams (Fig. 7). To improve the visibility of these diagrams we discarded connection lines that are recorded by fewer than 2 crystals from the individual Systems Analysis plots (Fig. 7). A total of 6 crystals (1 from *SET1*; 2 from *SET2* and 3 from *MtRs*) were affected by these reductions. We found 8 crystals that are homogeneous (Fo_{75-78}) without compositional zoning and are therefore also not displayed in the Systems Analysis plots. This explains why the number of connection lines (and therefore crystals) shown in Figure 7 (i.e. *188*) is less than the total number of crystals (i.e. *202*) analysed.

We could identify 6 different MEs that account for the compositional diversity observed in the 1669 olivines. Of these, two are so called '*core environments*' because the majority of the olivine cores have formed in them, i.e. M_1 (=Fo_{75-78}) and mm_1 (=Fo_{73-75}). The other four are '*rim environments*' in which the *SET1* and *SET2-MtRs* olivine rims crystallized, i.e. M_2 (=Fo_{70-72}), M_3 (=Fo_{65-69}), M_4 (=Fo_{60-65}) and M_5 (=Fo_{50-59}). Of these, M_3 and M_5 are dominant.

The thickness of the connections lines shown in Fig. 7a-c is directly linked to the number of crystals tracking a certain connectivity path (i.e. connection between two MEs). The majority of the MEs such as M_1 (=Fo_{75-78}), M_2 (=Fo_{70-72}) and mm_1 (=Fo_{73-75}) were already identified in the 1991-2008 olivines where it was found that these MEs are well-connected in the 'modern' plumbing system of Etna (Kahl *et al.,* 2015). On the other hand, more evolved environments such as M_3 (=Fo_{65-69}) were only occasionally identified in the 1991-2008 samples. In fact, the only recent samples possessing a dominant population of olivines recording a highly-evolved environment M_3 (=$Fo_{65\text{-}69}$) were those related to paroxysms (e.g. April 11, May 7 and September 9) of the 2007 summit activity. Given the scarcity of examples, the M_3 environment was previously believed to represent a transient, rarely sampled feature of the plumbing system (Kahl *et al.,* 2015). The 1669 products, by contrast, present abundant evidence (i.e. rim compositions of olivines; Fig. 5) that MEs containing highly-evolved magmas such as M_3 (=$Fo_{65\text{-}69}$), M_4 (=$Fo_{60\text{-}65}$) and M_5 (=$Fo_{50\text{-}59}$) could have played a major role in historical eruptions at Mt. Etna and are likely to represent long-term features of Etna's historic plumbing system. Highly-evolved environments environment such as M_4 (=$Fo_{60\text{-}65}$) and M_5 (=$Fo_{50\text{-}59}$) have not been shown to be involved in modern activity (Viccaro *et al.,* 2015; M. Pompilio pers. com.), implying that significant changes have occurred over historical time.

In the following paragraphs, we describe the connection history observed through the Systems Analysis of the 1669 eruption products and we discuss how connectivities change over time.

1669 SET1. In the *SET1* olivines we observe mainly two dominant connection patterns (Fig. 7a), interlinking the '*core environments*' M_1 (=$Fo_{75\text{-}78}$) and mm_1 (=$Fo_{73\text{-}75}$) with the highly evolved '*rim environment*' M_5 (=$Fo_{51\text{-}59}$). Besides the main connection routes M_1-M_5 (65 crystals) and mm_1-M_5 (23 crystals), there are minor routes connecting the environments M_1-M_4 (14 connections) and M_2-M_5 (7 connections).

1669 SET2. The *SET2* olivines also display two dominant populations (Fig. 7b) tracking the connections M_1-M_3 (33 crystals) and M_1-M_2 (17 crystals). Few crystals record the histories mm_1-M_2 (8 crystals) and mm_1-M_3 (6 crystals).

1669 MtRs. In this sample we find olivines that record fewer connections. We observe one population (8 crystals) that tracks the connection M_1-M_3 (Fig. 7c). Minor connections are related to the environments mm_1-M_2 (2 crystals) and M_1-mm_1 (2 crystals). The connection patterns in the

MtRs olivines show a close resemblance to those found in the *SET2* olivines (Fig. 7c), suggesting that the crystals contained in the *MtRs* and the *SET2* magmas experienced the same late-stage magmatic history.

In summary, from the combined Systems Analysis record of the 1669 samples, we find that the vast majority (96%) of the olivine cores record a common early stage magmatic history related to crystal growth or residence in the Magmatic Environments M_1 (=$Fo_{75\text{-}78}$; i.e. 139 crystals) and mm_1 (=$_{73\text{-}75}$; i.e. 42 crystals). The identification of four different '*rim environments*' [i.e. M_5 (=$Fo_{50\text{-}59}$; 98 crystals), M_4 (= $Fo_{60\text{-}65}$; 14 crystals), M_3 (=$Fo_{65\text{-}69}$; 47 crystals) and M_2 (=$Fo_{70\text{-}72}$; 27 crystals)] suggests diverging late stage magmatic histories in *SET1* vs. *SET2-MtRs* samples, following the formation of the olivine cores in the dominant environment M_1.

CHEMICAL & PHYSICAL CHARACTERISTICS OF MAGMA STORAGE

We applied thermodynamic calculations using the *rhyolite-MELTS* software (Gualda *et al.,* 2012; Ghiorso & Gualda, 2015) to characterize the MEs in which the cores and the different rims of the *SET1* and *SET2-MtRs* olivines formed.

Following the modelling procedure outlined in Kahl *et al.* (2015), we started with the identification of appropriate starting compositions (glass or whole rock) from which the most primitive olivine composition observed [i.e. M_1 (=$Fo_{75\text{-}78}$)] could have crystallized. The bulk composition of magma provides the largest source for variability. Therefore, we checked carefully the given range of bulk compositions (Table 3) for the *SET1, SET2* and *MtRs* samples. We find that each of these compositions could be in equilibrium with the most primitive olivine population ($Fo_{75\text{–}78}$) identified in the 1669 Etna eruption products.

In addition to major element chemistry, water contents and the prevalent oxygen fugacity conditions (fO_2) can have a significant impact on crystallization paths (e.g. Kahl *et al.,* 2015). Micro-analytical studies of olivine hosted melt inclusions (MIs) in the 1669 eruption products reveal variable, but low, total water contents (1.0 - 0.3 wt.%, e.g. Clocchiatti & Métrich, 1984; Métrich & Rutherford, 1998). The oxidation state of Etna lavas has been constrained by the type of Fe–Ti oxides present (e.g. Métrich & Clocchiatti, 1996; Kahl *et al.,* 2011), as well as through experimental studies (e.g. Pompilio & Rutherford, 2002), to lie in the vicinity of the Ni–NiO reaction (NNO) oxygen fugacity buffer.

The forward modelling strategy using the *rhyolite-MELTS* software (Gualda *et al.,* 2012; Ghiorso & Gualda, 2015) was defined as follows. We started with the melt compositions provided in Table 3 simulating fractional crystallization, following the demonstration by Kahl *et al.* (2015), that equilibrium crystallization cannot explain observed compositional diversity in modern Etna samples. Fractional crystallization was modelled along different fO_2 paths (QFM or NNO) for different initial water contents (1.5 wt% to dry). Finally, the P-T space was scanned along isobaric lines (3.0-0.5kbar) at a temperature range starting from liquidus down to 1050°C, in agreement with the lowest temperatures obtained by geothermometry (1070 ±20°C; 1081 ± 17°C, Kahl *et al.,* 2015) applying the geothermometer of Loucks (1996), at intervals of 5°C. The sets of conditions at which olivines corresponding to the different MEs could have formed are shown in figure 8 and the results of the MELTS simulations are summarized in SD Electronic Appendix 9. The applied conditions were considered plausible for a given ME only when the full compositional range of olivine corresponding to that ME (e.g. Fo_{75-78} for M_1) could be obtained.

At melt water contents ranging from dry to 1.1 wt.%, olivine compositions corresponding to the Magmatic Environment M_1 can be obtained at QFM or NNO, temperatures between 1060-

1170°C and pressures ≤ 1kbar (Fig. 8a-d). M_1 olivines typically coexist with clinopyroxene, plagioclase and Fe-Ti oxides with compositions that lie within the observed range of natural compositions (An_{56-85}, Corsaro *et al.,* 1996; $Mg\#_{73-93}$ and Mt_{35-52}, this study). At QFM, the obtained clinopyroxene compositions (i.e. $Mg\#_{81-83}$) match the mafic end of the observed natural compositions whereas the modelled plagioclase compositions (i.e. An_{66-75}) fall within the intermediate range of observed natural compositions. The simulated Fe-Ti oxide compositions (i.e. Mt_{35-38}) match the lower end of natural compositions. At NNO, the results are similar, with the distinction that the obtained Fe-Ti oxide compositions (i.e. Mt_{50-57}) fall outside the compositional range of observed Fe-Ti oxides.

These observations are in agreement with the results presented in Kahl *et al.* (2015). These authors found that M_1 olivines form at QFM or NNO, temperatures ≥1110°C and melt water contents between 0.1 and 1.4 wt.% coexisting with clinopyroxene ($Mg\#_{80-85}$), plagioclase (An_{50-83}) and Fe-Ti oxide (Mt_{45-58}), using a bulk rock composition of the 2002-2003 S-flank eruption of Mt. Etna (MgO content 8.17wt%) as the starting composition. M_1-type olivines coexisting with An-rich (An_{80-83}) plagioclase at QFM or NNO and low melt water contents could only be reproduced at low pressures between 0.25 and 0.75kbar. The only distinction to the results obtained in the present study is that M_1 olivines and Fe-Ti oxides could only coexist at oxygen fugacity conditions buffered at NNO (Kahl *et al.,* 2015).

Evolved olivine compositions corresponding to M_3 (=Fo_{65-69}) can be reproduced primarily under QFM conditions and lower temperatures (below 1140°C). M_3 olivines form at melt water contents ranging from dry up to 1.3wt% at all pressures considered (0.5- 3.0kbar) (Fig. 8a, c) together with clinopyroxene ($Mg\#_{74.5-78.4}$), plagioclase (An_{53-64}) and Fe-Ti oxide (Mt_{43-52}). At NNO, M_3 olivines form at high pressures (i.e. 2.0-3.0kbar; Fig. 8b) and dry conditions only, together with clinopyroxene (Mg# $_{74\text{-}79}$). Kahl *et al.* (2015) were able to reproduce M_3 olivines at QFM, low melt water contents (0.2-0.4 wt. %), temperatures below 1100°C and all pressures considered (0.5-3.0kbar) together with clinopyroxene, plagioclase and Fe-Ti oxides with the observed compositions.

The most evolved olivine compositions M_5 (=$Fo_{51\text{-}59}$) identified in the 1669 samples form at QFM only, under dry conditions, temperatures below 1100°C and pressures between 1.0 to 3.0kbar (Fig. 8a). At these conditions only clinopyroxene (Mg#74) forms with the observed compositions. Olivines of this composition could not be reproduced in the study of Kahl *et al.* (2015).

From our MELTS simulations we find that plagioclase is the liquidus phase of 1669 magmas at all pressures and water contents considered. We observe that An-rich plagioclase compositions (i.e. $An_{80\text{-}85}$) are not in equilibrium with any of the observed olivine populations and can form at pressures from 0.5 to 3.0kbar, melt water contents of 1.5 and 2.5 wt% (the latter for An_{85}) and temperatures between 1090-1144°C, irrespective of the oxygen fugacity conditions. The bulk of the more evolved plagioclase compositions (i.e. $An_{53\text{-}75}$), however, form in equilibrium with the observed olivine populations ($An_{53\text{-}64}$ with M_3; $An_{66\text{-}75}$ with M_1) but at lower melt water contents (dry to 1.3 wt.%). The most evolved olivine population M_5 does not coexist with plagioclase compositions in the observed range. We believe that the lower water contents, at which the bulk of the evolved plagioclase crystals form in equilibrium with the majority of the observed olivine and evolved clinopyroxene compositions, could be related to shallower depths reached by *SET1* and *SET2* magmas (P <800bars; e.g. Métrich & Rutherford, 1998). In summary, the observed differences in the MEs the olivines and their melts passed through are mainly related to changes in the melt water content, oxygen fugacity and temperature.

TIME-INTEGRATED APPROACH - DIFFUSION MODELLING

Following the approach outlined in Kahl *et al.* (2011 & 2013) we have modelled the diffusive relaxation of compositional zoning profiles in 150 olivines from *SET1* and *SET2* samples. The criteria for the choice of concentration profiles for modelling and tests for robustness have been reported in full detail in, e.g. Kahl *et al.* (2011 & 2013) and Costa *et al.* (2008). We note that the compositional zoning profiles preserved in olivines from the Monte Rossi (MtRs) bomb sample were not robust enough (i.e. weak zoning) for diffusion modelling and these crystals were therefore discarded. The application of diffusion modelling to the identified olivine populations allows us to (i) assess the timing and duration over which the crystals (plus their associated melts) have been transferred between the different MEs identified and (ii) reconstruct the residence times of the *SET1* and *SET2* magmas within different sections of the plumbing system prior to eruption.

Modelling approach

For our modelling approach, we made use of the following 1-D expression of the diffusion equation (i.e. Fick's 2nd law)

$$\frac{\partial C_i(x,t)}{\partial t} = \frac{\partial}{\partial t}\left(D_i \frac{\partial C_i(x,t)}{\partial x}\right) \qquad (1)$$

where C_i is the concentration of element i, x denotes the distance, D_i is the diffusion coefficient of element i, and t is time. The evolution of the concentration with time (t) at different spatial coordinates (x), C_i (x, t), is obtained numerically using a one-dimensional finite difference scheme. An example diffusion *Mathematica* code is provided as Supplementary Data (Electronic Appendix 9) of Kahl *et al.* (2015) but can be obtained from the authors. In this study, we focused predominantly on Fe-Mg zoning in olivine, using Fe-Mg diffusion coefficients obtained by

Dohmen *et al.* (2007a, b). Minor (Mn, Ca, Ni) and trace element (Al, P, Ti, Cr) profiles were obtained and carefully checked using EMP analysis and high-resolution LA-ICP-MS mapping (Ubide *et al.,* 2015; Fig. 6), but did not yield characteristic zoning patterns that could be used for diffusion modelling.

As diffusion of most elements in olivine is strongly orientation-dependent with respect to the crystal lattice, we have taken into account the effects of diffusion anisotropy. For this purpose, the orientation and the angular relation of the crystallographic a-, b- and c-axis in the analysed olivine crystals was determined using electron backscatter diffraction techniques EBSD (see Analytical methods for more details).

Input parameters - temperature & oxygen fugacity (fO_2)

Magmatic temperatures were determined using the Fe–Mg exchange geothermometer between coexisting clinopyroxene and olivine rims (Loucks, 1996) and were 1070 ± 20°C. The oxygen fugacity (fO_2) conditions were set to QFM, given that at this temperature range, thermodynamic calculations using *rhyolite-MELTS* (Gualda *et al.,* 2012; Ghiorso & Gualda, 2015) indicate that M_3- and M_5-type olivine cannot be formed at NNO (Kahl *et al.*, 2015).

Examples of calculated diffusion models that fit the concentration profiles are shown in Figure 9. Propagation of errors and uncertainties of the obtained timescales were performed following the procedure described in Kahl *et al.* (2015). A frequency distribution of all calculated timescales is shown in Figure 10a.

Timescale results

Applying the procedures outlined above we obtained 150 time estimates (*SET1*=109; *SET2*=41) from modelling the diffusive relaxation of Fe-Mg zoning profiles in 150 olivine crystals (Fig.

10a). A summary with all modelled timescales and the sequence of MEs as recorded in the chemical stratigraphy of the crystals is provided in Table 4. The observed distribution of timescales is fairly large ranging from a minimum of a few days up to a maximum of 1.5 years, with the majority (76%) to the obtained time estimates being shorter than 3 months (Fig. 10a). The observed array of timescales is in good agreement with results from recent Etna eruptions (e.g. Kahl *et al.,* 2011, 2013 & 2015) and other basaltic volcanoes (e.g. Albert *et al.,* 2015; Viccaro *et al.,* 2016c; Rae *et al.,* 2016; Hartley *et al.,* 2016). Corresponding timescales of *SET1* (red circles) and *SET2* (green squares) olivines are shown in Figure 10b. The horizontal bars represent the associated 1σ errors related to uncertainties from geothermometry (see Kahl *et al.,* 2015 for details on error propagation procedures).

1669 *SET1*. Time estimates related to the initial stages of the eruption (i.e. March 11 – 20, 1669) range from 16 days up to 1.5 years with the majority (61%) being shorter than 3 months (Fig. 10b).

1669 *SET2*. Time estimates related to the second half (i.e. post-March 29, 1669) of the eruptive activity are shifted towards slightly shorter timescales (10 days up to ~5 months) with the majority (71%) being shorter than 2 months (Fig. 10b).

Timing of magma transfer

Kahl *et al.* (2011, 2013 & 2015) demonstrated that that the application of Systems Analysis to populations of zoned olivine crystals can be used to uniquely link the compositional information preserved in the chemical stratigraphy of olivines with the transport dynamics of their associated melts. Extending this approach to the 1669 olivines enables us to decipher diverging magmatic histories in the *SET1* and *SET2-MtRs* olivines related to different magma transfer pathways connecting the '*core*' and the '*rim*' MEs. To get an idea of the timing and duration of magma transfer between these environments we have plotted the frequency of intrusive events as functions of the different migration routes identified in the Systems Analysis in Figure 11. The intrusion times have been re-calculated by successively subtracting the modelled olivine timescales from the assumed eruption dates of the *SET1* (i.e. March 19, 1669) and *SET2* (i.e. April 04, 1669) samples.

We observe that magma migration activity along the most prominent connection route M_1-M_5 (65 crystals; Fig. 7a), as recorded in the *SET1* olivines, occurs over a range of timescales from 16 days up to 1.5 years (Fig. 10b). The communication between the environments M_1 and M_5 started 1.5 years (October 1667) prior to eruption onset on March 11, 1669. Starting in October and becoming more frequent since November 1668, intrusion activity along this route re-kindled and continued until shortly before the onset of eruptive activity (Fig. 11). Magma transfer along other, minor routes such as mm_1-M_5 (26 crystals; Fig. 7a), M_1-M_4 (14 crystals; Fig. 7a) and M_2-M_5 (7 crystals; Fig. 7a) occurred over shorter timescales (22 days up to 8 months; Fig. 10b) starting between mid-October and early-November 1668, and becoming more frequent towards the eruption onset (Fig. 11). We also find that the magma migration activity along M_1 -M_5 ***decreased*** in the short term (i.e. days) before the onset of the eruption, as indicated by a decreasing number of crystals recording this event (Fig. 11).

The *SET2* olivines record a different late stage magmatic history, with the pathway M_1-M_3 (33 crystals; Fig. 7b) as the main transport route. Communication between the environments M_1 and M_3 commenced between mid- to late-November 1668 and was soon followed by mixing activities along other, minor routes such as M_1-M_2 (17 crystals; Fig. 7b), mm_1-M_2 (8 crystals; Fig. 7b) and mm_1-M_3 (6 crystals; Fig. 7b). Timescales related to these minor connection routes are shorter (13 days up to 3 months; Fig. 10b) and mixing occurred from mid-December 1668 (Fig. 11). Taking the number of crystals as evidence of intensity, we observe that the intrusive and mixing activity along all routes ***increased*** in the short-term (i.e. February 1669) both prior to and following the eruption onset (Fig. 11).

Occasionally, we also find rare olivine crystals (n=2) that record entrainment of ‘older’ olivine cores of more mafic composition, i.e. M_0 (=Fo_{79-82}, see Kahl *et al.,* 2015 for more details) from the surrounding crystal mush. These olivines are overgrown by more evolved rims of composition M_5 (=Fo_{51-59}) or M_2 (=Fo_{70-72}) and the corresponding timescales suggest that the crystals were entrained in their respective host melts sometime between late-December 1668 and mid-January 1669. This coincides with the observed trend of increasing magma migration and/or mixing activity and the development of a branched shallow magma transport system commencing in November 1668 and continuing until the eruption onset (Fig. 11), with two dominant but diverging magma pathways (M_1-M_5 and M_1-M_3) as recorded by the *SET1* and *SET2-MtRs* olivines.

PUTTING OBSERVATIONS INTO A MODEL: THE CHRONOLOGY OF MAGMATIC EVENTS

Combination of the information obtained from the Systems Analysis of the olivine zoning record and temporal information from modelling the diffusive relaxation of such zoning allows reconstruction of the sequence of magmatic events in the internal plumbing system of Etna volcano before and during the 1669 eruption. By considering the chemical stratigraphy preserved in 188 olivine crystals we can infer that olivine crystals resided in or interacted with six different Magmatic Environments (MEs) prior to eruption (Fig. 7).

We observe that the vast majority (74%) of the olivine cores are connected to the dominant Magmatic Environment M_1 (=Fo_{75-78}) whose existence can be tracked throughout all studied eruption products (i.e. *SET1*, *SET2-MtRs*). The occurrence of large olivine cores with compositional plateaux predominantly at Fo_{75-78} suggests, that the crystals have resided in M_1 for a significant period of time before moving on to other MEs. Furthermore, we find that these core compositional plateaux form groups or clusters in variation diagrams (Fig. 5e, g). Taking the extent of the observed compositional plateaux as evidence we infer that the instantaneous ambient conditions within M_1 were held constant during the crystallisation of olivine cores. Such constant conditions can exist for example within a large reservoir (e.g. sill or dyke) without large-scale convection. We suggest that a reservoir M_1 existed at shallow levels ($P \leq 1$kbar) within Etna's plumbing system containing a partially degassed melt (up to 1.1 wt %; ~5.1 wt% MgO) in equilibrium with olivine (Fo_{75-78}), clinopyroxene ($Mg\#_{81-83}$), plagioclase (An_{66-75}) and Fe-Ti oxide (Mt_{35-52} depending on the fO_2: QFM or NNO buffer) at temperatures ≤ 1170°C. The depth range (≤1kbar; ≤3km) at which M_1 olivine cores can be formed correlates with the top part of a main magma storage volume (Fig. 12a) that was identified between ~2km bsl down to 8-9km bsl (e.g. Patanè *et al.,* 2013; Bonaccorso *et al.,* 2011). This body lies along the western border of the high Vp velocity body (HVB) (Aloisi *et al.,* 2002; Patanè *et al.,* 2003, 2006) and is interpreted as the consensus main pathway for magma transport and magma accumulation at Mt. Etna (e.g. Patanè *et al.*, 2013).

The 1669 (*SET1* and *SET2-MtRs*) olivine rims are more diverse in composition, ranging from Fo_{51} to Fo_{78}, and form distinct trends in variation diagrams (Fig. 5d, f) indicating that the conditions under which the olivine rims formed were more variable. Our MELTS modelling results suggest that the *SET1* (M_5=Fo_{51-59}) and *SET2* (M_3=Fo_{65-69}) rim populations can be obtained over a much broader pressure range (0.5-3.0kbar) and variable water conditions (dry up to 1.3wt%). Taking these observations as evidence, we think that the *SET1* and *SET2-MtRs* olivine rims could reflect crystallization under polybaric conditions within two different environments M_5 and M_3, which are characterized by variable temperatures, water contents and oxygen fugacity conditions. Polybaric crystallisation of *SET1* and *SET2-MtRs* olivine rims agrees with findings from textural, compositional and thermobarometric studies of Etna plagioclase and clinopyroxene (Giacomoni *et al.,* 2014 & 2016; Armienti *et al.,* 2013). These studies suggest that clinopyroxene and plagioclase crystallization - although starting at different depths (Fig. 12b) - occurs continuously under polybaric conditions through a vertically-extended feeding system containing different magma crystallization levels (Giacomoni *et al.,* 2014 & 2016; Armienti *et al.,* 2013). The stability field of plagioclase and clinopyroxene further indicates a large variability of the water content within Etna's plumbing system (Giacomoni *et al.,* 2014 & 2016). This observation agrees with the variable water contents under which the different olivine rim and core populations identified in this and previous studies (Kahl *et al.,* 2015) could be obtained via thermodynamic modelling.

Combining the above observations with the temporal record, obtained from diffusion modelling of 150 olivine crystals, we can derive the following schematic scenario of magmatic events in the plumbing system of Mt. Etna that could have lead to the 1669 flank eruption:

We believe that after the formation of the olivine cores under relatively constant conditions, possibly within a larger reservoir M_1 located at relatively shallow levels (P ≤ 1kbar; ≤ 3km) within Etna's plumbing system, the reservoir was intruded by a batch of more evolved, degassed and possibly aphyric M_5-type magma (Fig. 12c). From the comprehensive timescale record (n=109) of the *SET1* olivines, we observe that intrusions into M_1 occurred as early as 1.5 years (October 1667) prior to the eruption onset. From October 1668, these injections became more frequent, and the *SET1* olivine rims began crystallizing. Due to the fact, that M_5 olivines only form rims, and never occur as cores in the *SET1* samples, plus considering the broad pressure range under which they can be formed, we suggest that the M_5 environment could represent a feeder dyke or conduit. *SET1* olivine rims grow in this conduit as it transects the M_1 reservoir and propagates further to the surface (Fig. 12c). This scenario would agree with the lack of M_5-type olivine cores and would also explain why the rims can be obtained over a broader pressure interval.

The steady replenishment of M_1 that initiated in October 1668 and continued until shortly before the eruption onset has probably fluidized and eroded the surrounding magma mush, resulting in the formation of a local "mixing bowl" (Bergantz *et al.,* 2015; Schleicher *et al.,* 2016) within the reservoir M_1. The formation of such a mixing bowl is evidenced by the core and rim compositions of a minor subset of olivines from the *SET1* samples, which refer to the MEs M_4 (=Fo60-65), M_2 (=Fo70-72) and mm_1 (=Fo73-75). The existence of such a local mixing bowl is further underpinned by the corresponding timescale determinations (Fig. 11). We observe, for example, that a major intrusive event (i.e. M_1-M_5) is followed by a delay of only a few days or weeks by a mixing (e.g. M_1-M_4) or entrainment (e.g. M_2-M_5 and mm_1-M_5), event involving a subset of crystal cores or rims that formed in these minor magmatic environments (Fig. 11). In this sense, we think that these minor ME connections identified in Systems analysis of the *SET1* olivines (Fig. 7a), refer to local mixing trajectories reflecting fluidization and/or mixing within the M_1 reservoir as time proceeds. Starting in November 1668, only a few weeks after the first intrusive episode into the M_1 reservoir, a second pulse of magma injections (M_3-type magma) is observed. However, this time the intrusive event is recorded by the *SET2* olivines, and marks the onset of simultaneous magma injections, along two different pathways (M_1-M_5 and M_1-M_3), into the mutual reservoir M_1 (Fig. 12d). The intrusion frequency of M_3-type magma into M_1 increased notably from December 1668, and is again followed by mixing activities along minor connection routes (Fig. 11). As mentioned before, the steady injections of M_3 have probably caused the formation of another, localised "mixing bowl" within M_1, in which the surrounding magma mush will be fluidized and eroded. This again is evidenced by a minor subset of core and rim populations recognized in the *SET2* (and *MtRs*) olivines [i.e. $mm_1(=Fo_{73-75})$, $M_2(=Fo_{70-72})$] and a short delay in the corresponding timescale record (Fig. 11). Similar to the M_5-type olivine rims observed in the *SET1* samples, we find that the M_3-type rims can form under variable conditions (i.e. temperature ≤1140˚, dry-1.3wt% water contents, pressure 0.5-3.0kbar). We assume therefore that the environment M_3 could represent a second feeder dyke in which the M_3-type olivine rims started to crystallize [possibly together with clinopyroxene ($Mg\#_{74-79}$), plagioclase (An_{53-64}) and Fe-Ti oxide (Mt_{43-52})] when the dyke hit the major reservoir M_1, where the previously formed olivine cores have been picked up (Fig. 12d).

The simultaneous recharge of the reservoir M_1, along the two different routes M_1 -M_5 and M_1 -M_3, increased steadily from November 1668 (evidenced by the large number of crystals tracking these events) and remained high in the weeks and days prior to the eruption onset on March 11, 1669 (Fig. 11). We observe, however, that in the immediate days before the eruption, the number of crystals recording the recharge of M_5 into M_1 decreased (Fig. 11). We speculate that the steady replenishment of M_1, in the months and weeks prior to the eruption, could have enhanced the build-up of overpressure inside the reservoir. This may have resulted in the opening of a new fracture system that gave rise to the development of a branched shallow feeder system with two dominant, but diverging, magma pathways (M_1-M_5 and M_1-M_3) facilitating the sequential transfer of magma into the main conduit system (Fig. 12d, e). We note that seismicity increased ca. 2 weeks (e.g. Mulas et al., 2016 and references therein; Tanguy and Patanè, 1996) before the eruption onset, and we suggest that this could be related to *SET1* magma intruding the main conduit system. Then, in the early hours of March 11, a dry fracture system opened on the south flank of Etna, between Mt. Frumento (2800m a.s.l.) and Piano San Leo (1200 m a.s.l.), enabling lateral draining of the *SET1* magma and starting the eruption (Mulas et al., 2016 and references therein) (Fig. 12e).

Following the eruption of the *SET1* samples, the injection frequency of M_3 into M_1 remained high and persisted throughout the eruption onset as recorded by the *SET2* olivines (Fig. 11). It appears that shortly after the eruption onset, the local magma transfer dynamics changed resulting in the disruption of the dominant pathway M_1-M_5, as indicated by a decreasing number of *SET1* olivines tracking this history. Instead, the pathway M_1-M_3 became a dominant feeder that promoted syn-eruptive recharge and mixing in the weeks following the eruption onset (Fig. 12e), resulting in the eruption of the *SET2* (and MtRs) magma.

We can only speculate about the causes for the change in transfer dynamics. One possible explanation could be a pressure-induced change of the local stress field caused by the system inflating with magma and repeated dyke injections (e.g. Bonafede & Danesi, 1997; Acocella & Neri, 2003) of M_3 into M_1. Alternatively, it could be that the supply of M_5 magma simply decreased, resulting in the interruption of the M_1-M_5 pathway.

We want to stress here that whilst the development of a branched feeder system is only one possible scenario that can account for the events recorded in the chemical stratigraphy of the 1669 olivines, it is not without precedent. Kahl *et al.* (2013) observed for the 2006 summit eruptions that differences in the connectivity patterns of zoned olivine populations existed for the July and October episodes. They proposed that these could have been due to fluctuations in the prevalent magma transport regime. They concluded that such short-term fluctuations - occurring within months from each other - could be associated with modifications of the shallow plumbing system; this would be an analogous event to that proposed for 1669. As further evidence, the olivine rims of *SET1* and *SET2* track divergent late-stage magmatic histories (M_1-M_5 and M_1-M_3) that are inconsistent with the progressive emptying of a mixed or hybrid reservoir.

CONCLUSIONS

We have applied a three-way integrated methodology linking a Systems Analysis with a time-integrated study of zoned olivine populations and a forward modelling approach using thermodynamic calculations with *rhyolite-MELTS* to constrain the nature and dynamics of magma transfer and magma mixing before and during the 1669 flank eruption of Etna volcano. System Analysis of the compositional zoning record preserved in 202 olivine crystals revealed the existence of three distinct Magmatic Environments (MEs) in which the majority of the olivine cores [M_1 (=Fo_{75-78})] and rims [i.e. M_5 (=Fo_{51-59}) and M_3 (=Fo_{65-69})] formed. Application of thermodynamic calculations with the *rhyolite-MELTS* software enabled constraint of the key intensive variables associated with these MEs. We found that temperature, water content and oxidation state are the main distinguishing features of the different MEs.

Olivine cores (~Fo75-78) formed in a partially degassed environment M_1 together with clinopyroxene ($Mg\#_{81-83}$), plagioclase (An_{66-75}) and, depending on the fO_2 (QFM or NNO), Fe-Ti oxide (Mt_{35-52}), at temperatures ≤ 1170°C and pressures <1kbar. The different rim populations identified in the *SET1* and *SET2-MtRs* olivines indicate diverging magmatic histories following the core formation, suggesting a bifurcated magma feeder system for the 1669 eruption. We find that *SET1* rims (i.e. Fo_{51-59}) can form under dehydrated and QFM oxygen fugacity conditions at temperatures <1100°C, in equilibrium with evolved clinopyroxenes ($Mg\#_{72-74}$). The less evolved *SET2* olivine rims (=Fo_{65-69}) can be obtained at QFM or NNO oxygen fugacity conditions, at temperatures ≤ 1140°C, under variable water contents (dry up to 1.3 wt.%), and together with clinopyroxene ($Mg\#_{74-79}$), plagioclase (An_{53-64}) and Fe-Ti oxide (Mt_{43-52}).

Importantly, olivine cores define compositional plateaux formed under relatively uniform conditions, whereas olivine rims define broad compositional ranges that can form over a broad pressure range (0.5-3.0kbar). This suggests that olivine cores formed under relatively constant conditions, possibly within a larger reservoir M_1 that was located at shallow levels (≤1kbar) within Etna's plumbing system, and olivine rims formed in dykes (M3 and M5) transecting the large M1 reservoir. These results reinforce the idea of a multi-level, vertically zoned feeding system at Mount Etna, where magma can continuously experience variable chemical-physical conditions.

Application of diffusion modelling to the zoned olivine crystals enabled us to reconstruct the timing and chronology of melt and crystal transfer prior to and during the 1669 flank eruption. We find that the pathway M_1-M_5 was established 1.5 years prior to eruptive activity. In addition, the parallel M_1-M_5 recharge increased notably in the months prior to eruption onset. For several weeks a bifurcated transport system with two dominant magma pathways developed along M_1-M_5 and M_1-M_3 dyke injections. Accompanied by vigorous seismicity, in the immediate days prior to eruption the local magma transfer dynamics changed and the M_1-M_5 recharge activity slowed down. M_1-M_3 recharge remained high and persisted throughout the eruption onset on March 11, which drained *SET1* lavas. In the weeks following the eruption onset, the pathway M_1-M_3 became the dominant feeder dyke promoting syn-eruptive recharge and mixing in the shallow plumbing system culminating in the eruption of the later *SET2* lavas.

In conclusion, the three-way integrated approach used in this study allows the reconstruction of the evolutionary history of a temporally remote and hazardous flank eruption not been accessible by means of conventional volcano monitoring techniques. Combination of pre-existing and state-of-the-art petrological tools enabled us to track the magmatic events that led to the 1669 eruption and to decipher changes in the local magma transfer dynamics that immediately preceded the eruption onset. Forward thermodynamic modelling linked with a time-integrated study, allowed us to recover pre- and syn-eruptive magma storage conditions and timescales within different magma reservoirs located in the shallow plumbing system of Mt. Etna. Most importantly, we demonstrate that the time elapsed between magma injections into the shallow plumbing system and accumulation and remobilization of eruptible magma is on the order of months to weeks only.

FUNDING

This work was supported by an ERC Advanced Grant EVOKES (247076) to DBD. M.K. acknowledges two postdoctoral research fellowship grants of the Deutsche Forschungsgemeinschaft (DFG) (KA 3532/1-1) and the Icelandic Centre for Research (Rannís) (152726-051). TU acknowledges funding from Science Foundation Ireland grant SFI/12/ERC/E2499.

ACKNOWLEDGMENTS

This paper has benefited greatly from comments by G. Bergantz, N. Métrich and an anonymous reviewer. We thank A. Lumsden and M. Wilson for the editorial handling of the manuscript and for helpful comments. We are grateful to D. Müller (LMU Munich), D. Aßbichler (LMU Munich), R. Walshaw and G. Lloyd (University of Leeds) for assistance with EMP, XRF and EBSD analysis. We wish to thank S. Chakraborty for useful suggestions and discussions of the manuscript.

REFERENCES CITED

Acocella, V. & Neri, M. (2003). What makes flank eruptions? The 2001 Etna eruption and its possible triggering mechanisms. *Bulletin of Volcanology* **65**, 517-529.

Albert, H., Costa, F. & Marti, J. (2015). Timing of Magmatic Processes and Unrest Associated with Mafic Historical Monogenetic Eruptions in Tenerife Island. *Journal of Petrology* **56**, 1945-1966.

Allard, P., Behncke, B., D'Amico, S., Neri, S. & Gambino, S. (2006). Mount Etna 1993-2005: Anatomy of an evolving eruptive cycle. *Earth Science Reviews* **78**, 85-114.

Aloisi, M., Cocina, O., Neri, G., Orecchio, B. & Privitera, E. (2002). Seismic tomography of the crust underneath the Etna volcano, Sicily. *Physics of the Earth and Planetary Interiors* **134**, 139-155.

Andronico, D., Branca, S., Calvari, S., Burton, M., Caltabiano, T., Corsaro, R.A., Del Carlo, P., Garfì, G., Lodato, L., Miraglia, L., Murè, F., Neri, M., Pecora, E., Pompilio, M., Salerno, G. & Spampinato, L. (2005). A multi-disciplinary study of the 2002-03 Etna eruption insights into a complex plumbing system. *Bulletin of Volcanology* **67**, 314-330.

Armienti, P., Innocenti, F., Petrini, R., Pompilio, M., Villari, L. (1988). Sub-aphyric alkali basalt from Mt. Etna: inferences on the depth and composition of the source magma. *Rend Soc It Mineralogy and Petrology* **43**, 877-891.

Armienti, P., Perinelli, C. & Putirka, K.D. (2013). A new model to estimate deep-level magma ascent rates with application to Mt. Etna (Sicily, Italy). *Journal of Petrology* **54**, 795-813.

Asimow, P. D. & Ghiorso, M.S. (1998). Algorithmic modifications extending MELTS to calculate sub-solidus phase relations. *American Mineralogist* **83**, 1127–1131.

Barbieri, M., Cristofolini, R., Delitala, M.C., Fornaseri, M., Romano, R., Taddeucci, A. & Tolomeo, L. (1993). Geochemical and Sr-isotope data on historical lavas of Mount Etna. *Journal of Volcanology and Geothermal Research* **56**, 57-69.

Behncke, B. & Neri, M. (2003). The July-August 2001 eruption of Mt. Etna (Sicily). *Bulletin of Volcanology* **65**, 461-476.

Bergantz, G.W., Schleicher, J.M. & Burgisser, A. (2015). Open-system dynamics and mixing in magma mushes. *Nature Geoscience* **8**, 793–796

Bonaccorso, A., Bonforte, A., Currenti, G., Del Negro, C., Di Stefano, A., Greco, F. (2011). Magma storage, eruptive activity and flank instability: Inferences from ground deformation and gravity changes during the 1993-2000 recharging of Mt. Etna volcano. *Journal of Volcanology and Geothermal Research* **200**, 245-254.

Bonafede, M. & Danesi, S. (1997). Near-field modifications of stress induced by dyke injection at shallow depth. *Geophysical Journal Int*ernational **130**,435-448.

Borelli, G.A. (1670). Historia et meteorologia incendii aetnaei anni 1669. *In Officina Dominici Ferri*, Reggio Calabria, 162 pp.

Branca, S. & Del Carlo, P. (2004). Eruptions of Mt. Etna during the past 3200 years: A revised compilation integrating the historical and stratigraphic records. In: Bonaccorso, A., Calvari, S., Coltelli, M., Del Negro, C. & Falsaperla, S. (eds.) *Mt. Etna: Volcano Laboratory. American Geophysical Union, Geophysical Monograph* **143**, 1-27.

Branca, S., Coltelli, M. & Groppelli, G. (2011). Geological evolution of a complex basaltic stratovolcano: Mt. Etna, Italy. *Italian Journal of Geosciences* **130**, 306-317.

Branca, S., De Beni, E. & Proietti, C. (2013). The large and destructive 1669 AD eruption at Etna volcano: reconstruction of the lava flow field evolution and effusion rate trend. *Bulletin of Volcanology* **75**, 694.

Branca, S. Azzaro, R., De Beni, E., Chester, D. & Duncan, A. (2015). Impacts of the 1669 eruption and the 1693 earthquakes on the Etna Region (Eastern Sicily, Italy): An example of recovery and response of a small area to extreme events. *Journal of Volcanology and Geothermal Research* **303**, 25-40.

Calvari, S., Coltelli, M., Neri, M., Pompilio, M. & Scribano, V. (1994). The 1991-1993 Etna eruption: chronology and lava flow-field evolution. *Acta Vulcanologica* **4**, 1-14.

Carrera, P. (1636). Il Mongibello descritto in tre libri. In Catania, nel Palazzo dell'Illustrissimo Senato, per Gio. Rossi, 204 pp.

Chester, D.K., Duncan, A.M., Guest, J.E. & Kilburn, C.R.J. (1985). *Mount Etna. The anatomy of a volcano*. Chapman and Hall, London.

Chew, D.M., Babechuk, M.G., Cogné, N., Mark, C., O'Sullivan, G., Henrichs, I., Doepke, D. & McKenna, C.A. (2016). (LA,Q)-ICPMS trace-element analyses of Durango and McClure Mountain apatite and implications for making natural LA-ICPMS mineral standards. *Chemical Geology* **435**, 35-48.

Clark, A.M. & Long, J.V.P. (1971). *The anisotropic diffusion of nickel in olivine*. In: Sherwood, J.N., Chadwick, A.V., Muir, W.M. & Swinton, F.L. (eds.) *Diffusion Processes*. Gordon and Breach, 511-521.

Clocchiatti, R. & Métrich, N. (1984). La cristallisation des pyroclastes des éruptions étnéennes de 1669 (Mt Rossi et 1892 (Mt Silvestri). Témoignages de contamination. *Bulletin of Volcanology* **47**, 908-928.

Clocchiatti, R., Joron, J.L. & Treuil, M. (1988). The role of selective alkali contamination in the evolution of recent historic lavas of Mt. Etna. *Journal of Volcanology and Geothermal Research* **34**, 241–249.

Condomines, M., Tanguy, J.C. & Michaud, V. (1995). Magma dynamics at Mount Etna: constraints from U–Th–Ra–Pb radioactive disequilibria and Sr isotopes in historical lavas. *Earth and Planetary Science Letters* **132**, 297–314.

Corsaro, R.A., Métrich, N., Allard, P., Andronico, D., Miraglia, L. & Fourmentraux, C. (2009). The 1974 flank eruption of Mount Etna: An archetype for deep dike-fed eruptions at basaltic volcanoes and a milestone in Etna's recent history. *Journal of Geophysical Research* **114**, B07204.

Corsaro, R.A., Miraglia, L. & Pompilio, M. (2007). Petrologic evidence of a complex plumbing system feeding the July-August 2001 eruption of Mt. Etna, Sicily, Italy. *Bulletin of Volcanology* **69**, 401–421.

Corsaro, R.A., Cristofolini, R. & Patanè, L. (1996). The 1669 eruption at Mount Etna: chronology, petrology and geochemistry, with inferences on the magma sources and ascent mechanisms. *Bulletin of Volcanology* **58**, 348-358.

Costa, F. & Chakraborty, S. (2004). Decadal time gaps between mafic intrusion and silicic eruption obtained from chemical zoning patterns in olivine. *Earth and Planetary Science Letters* **227**, 517–530.

Costa, F., Dohmen, R. & Chakraborty, S. (2008). Timescales of magmatic processes from modelling the zoning patterns of crystals. *Reviews in Mineralogy and Geochemistry* **69**, 545–594.

Deer, W.A., Howie, R.A. & Zussman, J. (2013). An Introduction to the Rock-Forming Minerals. Mineralogical Society of Great Britain and Ireland, 510 pp.

Doglioni, C., Innocenti, F. & Mariotti, G. (2001). Why Mt. Etna? *Terra Nova* **13**, 25–31.

Dohmen, R., Becker, H.-W. & Chakraborty, S. (2007a). Fe–Mg diffusion in olivine I: experimental determination between 700 and 1,200°C as a function of composition, crystal orientation and oxygen fugacity. *Physics and Chemistry of Melts* **34**, 389–407.

Dohmen, R. & Chakraborty, S. (2007b). Fe–Mg diffusion in olivine II: point defect chemistry, change of diffusion mechanisms and a model for calculation of diffusion coefficients in natural olivine. *Physics and Chemistry of Minerals* **34**, 409–430.

Ferlito, C., Viccaro, M., Nicotra, E. & Cristofolini R. (2012). Regimes of magma recharge and their control on the eruptive behaviour during the 2001-2005 period at Mt. Etna (Italy). *Bulletin of Volcanology* **74**, 533-543.

Ferrara, F. (1818). Descrizione dell'Etna con la storia delle eruzioni e il catalogo dei prodotti. Palermo presso Lorenzo Dato, 256 pp.

Giacomoni, P.P., Ferlito, C., Coltorti, M., Bonadiman, C. & Lanzafame, G. (2014). Plagioclase as archive of magma ascent dynamics on "open conduit" volcanoes: The 2001–2006 eruptive period at Mt. Etna. *Earth-Science Reviews* **138**, 371-393.

Giacomoni, P.P., Coltorti, M., Bryce, J.G., Fahnestock, M.F. & Guitreau, M. (2016). Mt. Etna plumbing system revealed by combined textural, compositional, and thermobarometric studies in clinopyroxenes. *Contributions to Mineralogy and Petrology* **171**, 34.

Ghiorso, M.S. & Sack, R.O. (1995). Chemical mass transfer in magmatic processes. IV. A revised and internally consistent thermodynamic model for the interpolation and extrapolation of liquid–solid equilibria in magmatic systems at elevated temperatures and pressures. *Contributions to Mineralogy and Petrology* **119**, 197–212.

Ghiorso, M.S. & Gualda, G.A.R. (2015). An H2O-CO2 mixed fluid solubility model compatible with rhyolite-MELTS. *Contributions to Mineralogy and Petrology* **169**, 53.

Gillot, P.Y., Kieffer, G. & Romano, R. (1994). The evolution of Mount Etna in the light of potassium-argon dating. *Acta Vulcanologica* **5**, 81-87.

Gualda, G.A.R., Ghiorso, M.S., Lemons, R.V. & Carley, T.L. (2012). Rhyolite-MELTS: A modified calibration of MELTS optimized for silica-rich, fluid-bearing magmatic systems. *Journal of Petrology* **53**, 875-890.

Guest, J.E. & Duncan, A.M. (1981). Internal plumbing of Mount Etna. *Nature* **290**, 584-586.

Gvirtzman, Z. & Nur, A. (1999). The formation of Mount Etna as the consequence of slab rollback. *Nature* **401**, 782-785.

1175 Hartley, M.E., Morgan, D.J., Maclennan, J., Edmonds, M. & Thordarson, T. (2016). Tracking timescales of short-term precursors to large basaltic fissure eruptions through Fe–Mg diffusion in olivine. *Earth and Planetary Science Letters* **439**, 58–70.

1178 Hughes, J.W., Guest, J.E. & Duncan, A.M. (1990). *Changing styles of effusive eruption on Mount Etna since AD 1600*. In: Ryan, M.P. (ed.) *Magma transport and storage*. Wiley, New York, 385– 405.

1181 Jochum, K.P., Weis, U., Stoll, B., Kuzmin, D., Yang, Q., Raczek, I., Jacob, D.E., Stracke, A., Birbaum, K., Frick, D.A., Günther, D. & Enzweiler, J. (2011). Determination of reference values for NIST SRM 610-617 glasses following ISO guidelines. *Geostandards and Geoanalytical Research* **35**, 397–429.

1185 Kahl, M., Chakraborty, S., Costa, F. & Pompilio, M. (2011). Dynamic plumbing system beneath volcanoes revealed by kinetic modelling and the connection to monitoring data: an example from Mt. Etna. *Earth and Planetary Science Letters* **308**, 11–22.

1188 Kahl, M., Chakraborty, S., Costa, F., Pompilio, M., Liuzzo, M. & Viccaro, M. (2013). Compositionally zoned crystals and real-time degassing data reveal changes in magma transfer dynamics during the 2006 summit eruptive episodes of Mt. Etna. *Bulletin of Volcanology* **75**, 692.

1192 Kahl, M., Chakraborty, S., Pompilio, M. & Costa, F. (2015). Constraints on the Nature and Evolution of the Magma Plumbing System of Mt. Etna Volcano (1991–2008) from a Combined Thermodynamic and Kinetic Modelling of the Compositional Record of Minerals. *Journal of Petrology* **56**, 2025-2068.

Landi, P., Francalanci, L., Pompilio, M., Rosi, M., Corsaro, R.A., Petrone, C.M., Nardini, I. & Miraglia, L. (2006). The December 2002–July 2003 effusive event at Stromboli volcano, Italy: an insight into the shallow plumbing system by petrochemical studies. *Journal of Volcanology and Geothermal Research* **155**, 263–284.

Lanzafame, G., Neri, M., Acocella, V., Billi, A., Funiciello, R. & Giordano, G. (2003). Structural features of the July-August 2001 Mount Etna eruption: evidence for a complex magma supply system. *Journal of the Geological Society of London* **160**, 531-544.

Larrea, P., França, Z., Lago, M., Widom, E., Galé, C. & Ubide, T. (2013). Magmatic processes and the role of antecrysts in the genesis of Corvo Island (Azores Archipelago, Portugal). *Journal of Petrology* **54**, 769–793.

Loucks, R.R. (1996). A precise olivine–augite Mg–Fe-exchange geothermometer. *Contributions to Mineralogy and Petrology* **125**, 140–150.

Lundgren, P., Berardino, P., Coltelli, M., Fornaro, G., Lanari, R., Puglisi, G., Sansosti, E. & Tesauro, M. (2003). Coupled magma chamber inflation and sector collapse slip observed with synthetic aperture radar interferometry on Mt. Etna volcano. *Journal of Geophysical Research* **108**, 2247–2267.

Mancino, C. (1669). Narrativa del fuoco uscito da Mongibello il dì undici di marzo del 1669. Messina, Giuseppe Bisagni.

Métrich, N. & Clocchiatti, R. (1989). Melt inclusion investigation of the volatile behaviour in historic alkali basaltic magmas of Etna. *Bulletin of Volcanology* **51**, 185-198.

Métrich, N. & Clocchiatti, R. (1996). Sulphur abundance and its speciation in oxidized alkaline melts. *Geochimica et Cosmochimica Acta* **60**, 4151–4160.

Métrich, N. & Rutherford, M.J. (1998). Low pressure crystallization paths of H2O-saturated basaltic-hawaiitic melts from Mt Etna: Implications for open-system degassing of basaltic volcanoes. *Geochimica et Cosmochimica Acta* **62**, 1195–1205.

Métrich, N., Allard, P., Spilliaert, N., Andronico, D. & Burton, M. (2004). 2001 flank eruption of the alkali and volatile-rich primitive basalt responsible for Mount Etna's evolution in the last three decades. *Earth and Planetary Science Letters* **228**, 1-17.

Mulas, M., Cioni, R., Andronico, D. & Mundula, F. (2016). The explosive activity of the 1669 Monti Rossi eruption at Mt. Etna (Italy). *Journal of Volcanology and Geothermal Research* **328**, 115-133.

Murru, M., Montuori, C., Wyss, M., Privitera, E. (1999). The locations of magma chambers at Mt. Etna, Italy, mapped by b-values. *Geophysical Research Letters* **26**, 2553–2556.

Nicotra, E. & Viccaro, M. (2012). Unusual magma storage conditions at Mt. Etna (Southern Italy) as evidenced by plagioclase megacryst-bearing lavas: implications for the plumbing system geometry and summit caldera collapse. *Bulletin of Volcanology* **74**, 795–815.

Patanè, D., De Gori, P., Chiarabba, C. & Bonaccorso, A. (2003). Magma ascent and teh pressuraisation of Mt. Etna's volcanic system. *Science* **299**, 2061–2063.

Patanè, D., Barberi, G., Cocina, O., De Gori, P. & Chiarabba, C. (2006). Time resolved seismic tomography detects magma intrusions at Mount Etna. *Science* **313**, 821–825.

Patanè, D., Aiuppa, A., Aloisi, M., Behncke, B., Cannata, A., Coltelli, M., Di Grazia, G., Gambino, S., Gurrieri, S., Mattia, M. & Salerno, G. (2013). Insights into magma and fluid transfer at Mount Etna by a multiparametric approach: A model of the events leading to the 2011 eruptive cycle. *Journal of Geophysical Research - Solid Earth* **118**, 3519–3539.

Paton, C., Hellstrom, J., Paul, B., Woodhead, J. & Hergt, J. (2011). Iolite: freeware for the visualization and processing of mass spectrometric data. *Journal of Analytical Atomic Spectrometry* **26**, 2508–2518.

Pompilio, M. & Rutherford, M. J. (2002). Pre-eruption conditions and magma dynamics of recent amphibole-bearing Etna basalt. American Geophysical Union, Fall Meeting 2002, Abstracts V61A-1354.

Prior, D. J., Boyle, A. P., Brenker, F., Cheadle, M. C., Day, A., Lopez, G., Peruzzo, L., Potts, G. J., Reddy, S., Spiess, R., Timms, N. E., Trimby, P., Wheeler, J. & Zetterstrom, L. (1999). The application of electron backscatter diffraction and orientation contrast imaging in the SEM to textural problems in rocks. *American Mineralogist* **84**, 1741–1759.

Rae, A.S.P., Edmonds, M., Maclennan, J., Morgan, D., Houghton, B., Hartley, M.E. & Sides, I. (2016). Time scales of magma transport and mixing at Kilauea Volcano, Hawai'i. *Geology*, **44**, 463-466.

Recupero, G. (1815). Storia naturale e generale dell'Etna. Stamperia della Regia Università degli Studi, Catania, doi:10.3931/e-rara-11880.

Rittmann, A. (1965). Notizie sull'Etna. Supplemento al *Nuovo Cimento* **3**(I), 1117–1123.

Sakyi, P.A., Tanaka, R., Kobayashi, K. & Nakamura, E. (2012). Inherited Pb isotopic records in olivine antecryst-hosted melt inclusions from Hawaiian lavas. *Geochimica et Cosmochimica Acta* **95**, 169–195.

Schleicher, J.M, Bergantz, G.W., Breidenthal, R.E. & Burgisser, A. (2016). Time scales of crystal mixing in magma mushes. *Geophysical Research Letters* **43**, 1543–1550.

Schiano, P., Clocchiatti, R., Ottolini, L. & Busà, T. (2001). Transition of Mount Etna lavas from a mantle-plume to an island-arc magmatic source. *Nature* **412**, 900-904.

Spilliaert, N., Allard, P., Métrich, N. & Sobolev, A.V. (2006). Melt inclusion record of the conditions of ascent, degassing and extrusion of volatile-rich alkali basalt during the powerful 2002 flank eruption of Mount Etna (Italy). *Journal of Geophysical Research* **111**, B04203.

Stevens, N.F., Murray, J.B., Wadge, G. (1997). The volume and shape of the 1991-1993 lava flow field at Mount Etna, Sicily. *Bulletin of Volcanology* **58**, 449-454.

Tanguy, J.C. (1980). L'Etna: étude pétrologique et paléomagnetique: implications volcanologiques, 618 p. PhD thesis, University of Paris.

Tanguy, J.C. & Clocchiatti, R. (1984). The etnean lavas, 1977-83: petrology and mineralogy. *Bulletin of Volcanology* **47**, 879-894.

Tanguy, J.C. & Patanè, G. (1996). *L'Etna et le monde des volcans*. Diderot Editeur Paris, France.

Tanguy, J.C., Condomines, M., Le Goffe, M., Chillemi, V., La Delfa, S. & Patanè G. (2007). Mount Etna eruptions of the last 2,750 years: revised chronology and location through archeomagnetic and 226Ra-230Th dating. *Bulletin of Volcanology* **70**, 55–83.

Ubide, T., Arranz, E., Lago, M., Galé, C. & Larrea, P. (2012). The influence of crystal settling on the compositional zoning of a thin lamprophyre sill: a multimethod approach. *Lithos* **132 – 133**, 37-49.

Ubide, T., Galé, C., Larrea, P., Arranz, E. & Lago, M. (2014). Antecrysts and their effect on rock compositions: the Cretaceous lamprophyre suite in the Catalonian Coastal Ranges (NE Spain). *Lithos* **206–207**, 214-233.

Ubide, T., McKenna, C.A., Chew, D.M. & Kamber, B.S. (2015). High-resolution LA-ICP-MS trace element mapping of igneous minerals: In search of magma histories. *Chemical Geology* **409**, 157-168.

Viccaro, M., Giacomoni, P.P., Ferlito, C. & Cristofolini, R. (2010). Dynamics of magma supply at Mt. Etna volcano (Southern Italy) as revealed by textural and compositional features of plagioclase phenocrysts. *Lithos* **116**, 77-91.

Viccaro, M., Calcagno, R., Garozzo, I., Giuffrida, M. & Nicotra, E. (2015). Continuous magma recharge at Mt. Etna during the 2011–2013 controls the style of volcanic activity and compositions of erupted lavas. *Mineralogy and Petrology* **109**, 67–83.

Viccaro, M., Zuccarello, F., Cannata, A., Palano, M. & Gresta S. (2016a). How a complex basaltic volcanic system works: constraints from integrating seismic, geodetic, and petrological data at Mount Etna volcano during the July-August 2014 eruption. *Journal of Geophysical Research – Solid Earth* **121**, 5659-5678.

Viccaro, M., Barca, D., Bohrson, W.A., D'Oriano, C., Giuffrida, M., Nicotra, E. & Pitcher, B.W. (2016b). Crystal residence times from trace element zoning in plagioclase reveal changes in magma transfer dynamics at Mt. Etna during the last 400 years. *Lithos* **248-251**, 309-323.

Viccaro, M., Giuffrida, M., Nicotra, E. & Cristofolini, R. (2016c). Timescales of magma storage and migration recorded by olivine crystals in basalts of the March-April 2010 eruption at Eyjafjallajökull volcano, Iceland. *American Mineralogist* **101**, 222-230.

FIGURE CAPTIONS

Fig. 1 (a) Location and geodynamic setting of Mt. Etna with respect to the Apennine subduction front, the Malta escarpment (dashed line) and the subduction-related Aeolian island arc to the north. (b) Digital map of the S-flank of Mt. Etna illustrating the spatial distribution of the 1669 lava flow front and the progressive opening of the eruptive fissures (*1-5*). The different lava flow units are illustrated in distinct colours to highlight the temporal evolution of the flow field. Sample localities of the *SET1* (1-6/10) and *SET2* (2-1/5) lava flows and the *MtRs* bomb are marked with asterisks.

Fig. 2 Electron backscatter diffraction (EBSD) mapping of olivine. (a-b) False colour Backscatter electron (BSE) images of olivine crystals that erupted during the second half (i.e. *SET2*) of the 1669 flank eruption. (c-d) Electron backscatter diffraction (EBSD) maps of the same crystals (i.e. 1669 *SET2* 2-1 Ol-6 and 2-4 Ol-6). Different colours in the corresponding EBSD maps refer to different orientations of the three measured Euler angles indicating different orientations of the crystallographic a-, b- and c-axis in the olivines. Note that the application of EBSD mapping makes it possible to distinguish individual crystals. Individual step sizes used for the EBSD orientation maps are: 22.56µm for *2-1 Ol-6* and 20.88µm for *2-4 Ol-6*.

Fig. 3 (a) Total alkali vs. silica diagram (wt.%) of 1669 samples studied by Corsaro *et al.* (1996) and from this study (*SET1*: filled diamond; *SET2*: triangle; *MtRs*: circle). (b-l) Major element concentrations of whole rocks of *SET1*, *SET2* and *MtRs* samples of this study and of Corsaro *et al.* (1996).

Fig. 4 Illustration of the most common zoning types identified in the 1669 olivine crystals. Columns: Rim to core and rim to rim zoning profiles; Arrows in BSE images display direction of electron microprobe traverse. Rows: Zoning types as functions of eruption phases: *SET1*, *SET2* and *MtRs*. Bottom row: Displays complexities of the different zoning types as identified in 1991-93 samples (Kahl *et al.,* 2015). Fo: Forsterite; Fo=100*(Mg/[Mg+Fe]). (a) Type IV, normally zoned crystals with cores at Fo_{75-78} and rims at ~Fo_{55} (*SET1*) or ~Fo_{70} (*SET2* and *MtRs*). (b) Type VII, normal zoning with core at Fo_{73-75} and variable rims. Placeholders indicate that a particular zoning type could not be identified in the corresponding eruption product(s).

Fig. 5 (a-b) Frequency histograms of core and rim compositions of 202 olivine crystals erupted during the 1669 flank eruption. (c-d) MnO versus Forsterite content of olivine cores and rims. (e-f) CaO versus Forsterite content of olivine cores and rims. (g-h) MnO versus CaO plots of core and rim compositions. Coloured areas: Compositional range of the 5 different olivine populations identified in the 1991-2008 eruption products (Kahl *et al.,* 2015). Fo: Forsterite, Fo=100*(Mg/[Mg+Fe]).

Fig. 6 LA-ICP-MS element maps for Ni, Mn, Sc and P on representative olivine crystals from *SET1*, *SET2* and *MtRs* samples. Mapped areas are marked with white rectangles on false colour BSE images (black arrows indicate the direction of the electron microprobe traverses). LA-ICP-MS maps are constructed with the Iolite module 'Images from integrations' using 'Cold Warm' colour scales.

Fig. 7 Individual Systems Analysis diagrams of zoning patterns recorded in a total of 188 olivine crystals contained in the *SET1* (a), *SET2* (b) and *MtRs* (c) samples of the 1669 eruption. The number of olivine zoning patterns depicted in the Systems Analysis plots is smaller than the total number of crystals investigated (n=202). Minor connection lines recorded by only one crystal have been removed to improve visibility. Each coloured box represents a different Magmatic Environment (ME) as identified based on the six different olivine core and rim populations.

Connection lines between these MEs represent zoning patterns recorded in populations of olivine crystals. The variable thickness of the connection lines refers to the number of crystals tracking certain connectivities. The corresponding numbers are given next to each connection line. The arrows indicate the direction of the zoning patterns as recorded in the olivine crystals (arrow heads point in the direction of olivine rims).

Fig. 8 Olivine compositions (Fo mol%) obtained from fractional crystallization (FC) simulations using *rhyolite-MELTS* (Gualda *et al.,* 2012; Ghiorso and Gualda, 2015). The simulations were performed using the bulk rock compositions shown in Table 3 at the quartz–fayalite–magnetite (QFM) and the Ni–NiO (NNO) oxygen buffers, and variable water contents (dry to 1.5 wt% water). Vertical axis: crystallization temperature in degrees Celsius; horizontal axis: forsterite content. Filled squares: olivine compositions obtained for a given isobaric cooling path. M_1, M_3 and M_5: compositional range of olivine core and rim populations characterizing the dominant 'core' [i.e. M_1 (= $Fo_{75–78}$)] and 'rim forming' [i.e. M_3 (= Fo_{65-69}) and M_5 (= Fo_{51-59})] environments.

Fig. 9 Diffusion model fits. (a-d) False colour BSE images of representative olivine crystals. Black lines: Directions of EMP traverses. (e-h) Core to rim concentration profiles of olivine crystals erupted during the 1669 flank eruption of Mt. Etna. Blue circles: EMP traverses showing concentration profiles for Forsterite [100*Mg/ (Mg+Fe), in mol%]. Black stippled lines: Initial conditions; Red lines: Best fit diffusion models for the observed zoning profiles. Numbers in days indicate diffusive timescales obtained from best fit model solutions. M_1, M_3, M_4 and M_5 indicate core and rim formation within distinct Magmatic Environments. (i-l) Stereographic lower hemisphere plots depicting the angular relations between the major crystallographic directions (a-

, b- and c-axis) in olivine and the directions of the analytical traverses. Olivine orientation data were obtained using EBSD technique (see *Methods* section for full details).

Fig. 10 Comprehensive timescale record obtained from modelling the diffusive modification of Fe-Mg concentration profiles preserved in a total of 150 olivine crystals that fulfilled the robustness criteria described in Kahl *et al.* (2011) and Costa *et al.* (2008). (a) Frequency distribution of timescales for *SET1* (gray) and *SET2* (green) olivine crystals. Bin size: 20 days. (b) Compilation of calculated timescales as a function of crystal number including 1σ uncertainties arising from geothermometry. Coloured symbols refer to mixing timescales obtained from modelling individual *SET1* (gray diamonds) and *SET2* (green triangles) olivines. Modelling parameters: T=1070±20°C and fO_2=QFM. Diffusion models performed in this study used the Fe-Mg inter-diffusion coefficients provided by Dohmen *et al.* (2007a, b). No diffusion timescales for *MtRs* olivines were obtained, as EMP profiles did not fulfil robustness criteria.

Fig. 11 Calculated timescales of intrusive events into Etna's shallow plumbing system along different transport routes. Coloured symbols refer to individual intrusion times along different transport pathways calculated by subtracting the mixing timescales from the eruption dates of *SET1* (i.e. March 19, 1669) and *SET2* (i.e. April 04, 1669) samples. Black symbols refer to intrusion times related to rarely connected MEs such as M_0-M_5; M_0-M_2 and M_2-M_3 [M_0 (=Fo_{79-83}), not displayed in Figure 7]. Red dashed line (E) marks the overall eruption onset (i.e. March 11, 1669); Shaded area indicates the approximate range of seismic activity preceding the onset of the 1669 eruption. Contemporary records report that vigorous seismicity preceded the eruption by approximately two weeks and that earthquake intensity increased in the days (starting on March 8, 1669) prior to the eruption onset (e.g. Mulas *et al.,* 2016 and references therein).

Fig. 12 (a) Schematic illustration depicting the approximate depth of the reservoir M_1 and the dyke-like environments M_5 and M_3 in which the *SET1* (M_5) and the *SET2-MtRs* (M_3) olivine rims formed. Inserts list the physical conditions of the three environments obtained by thermodynamic modelling using *rhyolite-MELTS*. For comparison the depths contours of the high Vp velocity body (HVB; [8] Aloisi et al., 2002; [9-10] Patanè *et al.*, 2003 & 2006) and the consensus main magma pathway (grey arrow) (e.g. [11] Patanè *et al.*, 2013) are shown. (b) Schematic reconstruction of Etna's vertical feeding system (from Giacomoni *et al.*, 2014, 2016) from plagioclase and clinopyroxene crystallisation depths ([1] Giacomoni *et al.*, 2014; [2] Giacomoni *et al.,* 2016; [3] Armienti *et al.,* 2013). Vertical bars represent the depth range of low-velocity zones detected by [4] Bonaccorso *et al*. (2011), [5] Lundgren *et al.* (2003) and [6] Murru *et al.* (1999). For comparison the major stratigraphic units (AFM: Apennine Maghrebian folds; HB: Hyblean Platform; UC: Upper Crust) underlying Mt. Etna are shown. (c-e) Schematic reconstruction of the sequence and chronology of magmatic events in the internal plumbing of Mt. Etna before and during the 1669 flank eruption. (c) Dyke intrusions of M_5-type magma into the major reservoir M_1 (=Fo_{75-78}) commenced 1.5 years prior to the eruption onset. Since October 1668 repeated dyke injections of M_5 into M_1 resulting in the formation of the *SET1* olivine rims. (d) Starting in November 1668, a new batch of magma (M_3-type) intruded the reservoir M_1 as recorded in the chemical stratigraphy of the *SET2* olivines. Intrusions of M_3-type magma into M_1 resulted in the formation of the *SET2* olivines rims. In the months and weeks prior to the eruption, simultaneous injections of M_5- and M_3-type magma into the M_1 reservoir occurred and continued until the eruption onset. A branched feeder system with two dominant but diverging magma transport routes M_1-M_5 and M_1-M_3 developed. (e) Change of magma transport dynamics shortly after the beginning of the 1669 flank eruption resulting in the disruption of the pathway M_1-M_5 and the stabilisation of the transport route M_1-M_3, that facilitated syn-eruptive magma recharge and magma mixing in the weeks following the eruption onset. See main text for more details.

TABLE CAPTIONS

Table 1 Summary of 17th century flank activity

Table 2 Sample locations

Table 3 Bulk rock compositions of *SET1*, *SET2* and *MtRs* eruption products

Table 4 Comprehensive timescale record of *SET1* and *SET2* olivines

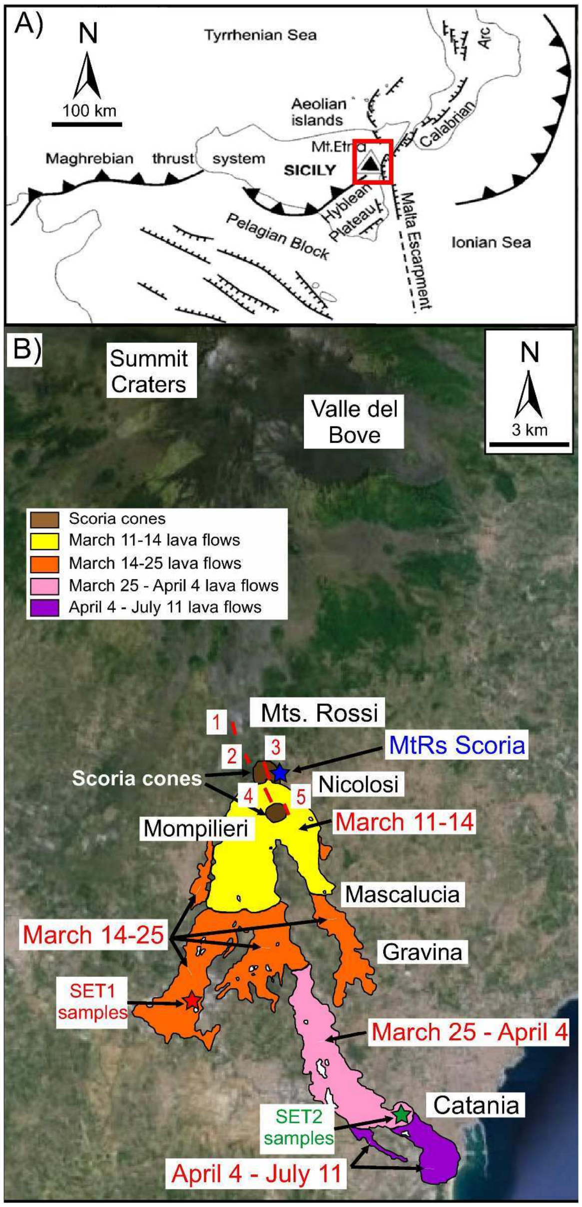

Figure 1

201x418mm (300 x 300 DPI)

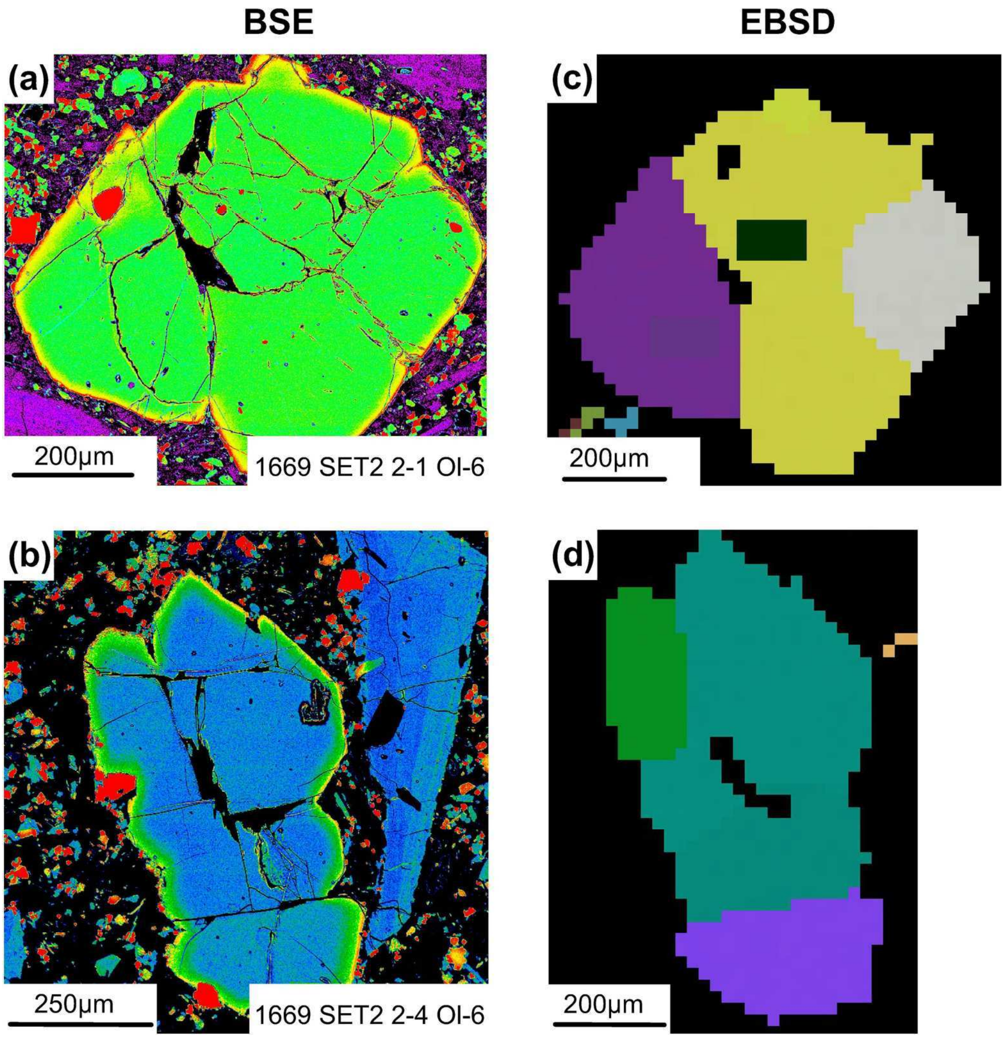

Figure 2

166x171mm (300 x 300 DPI)

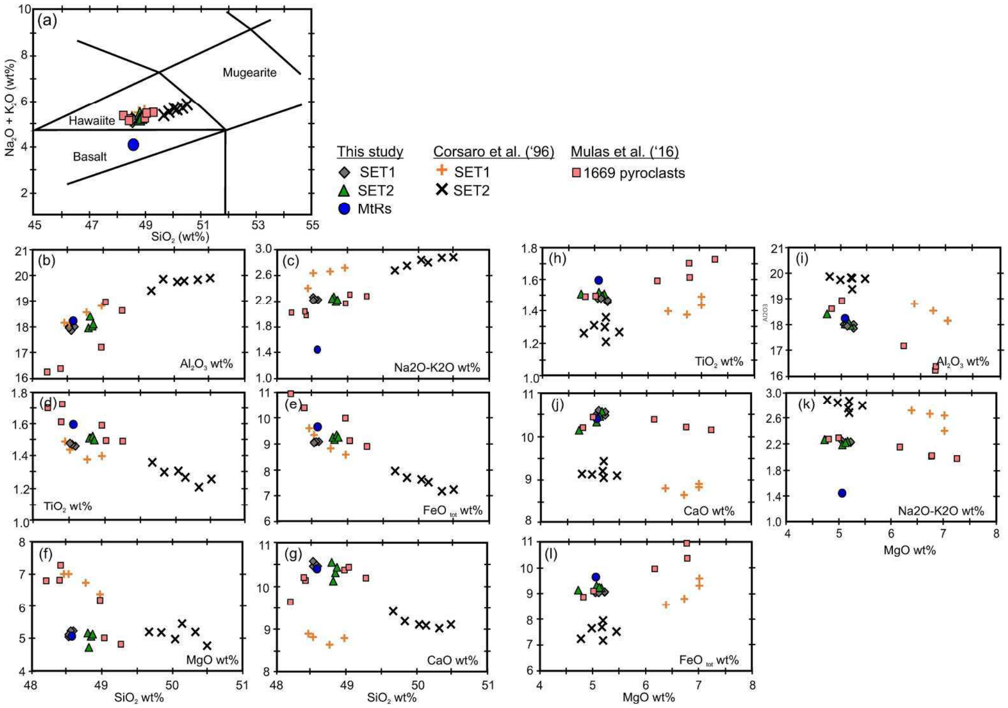

Figure 3

203x142mm (300 x 300 DPI)

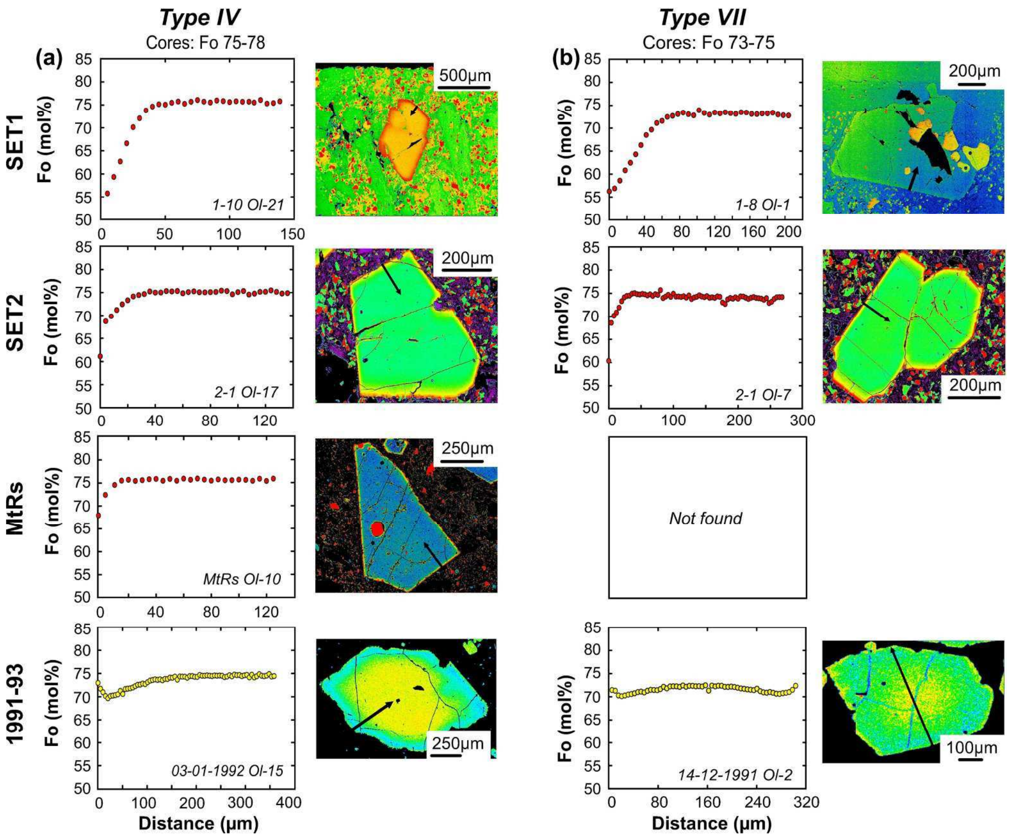

Figure 4

206x170mm (300 x 300 DPI)

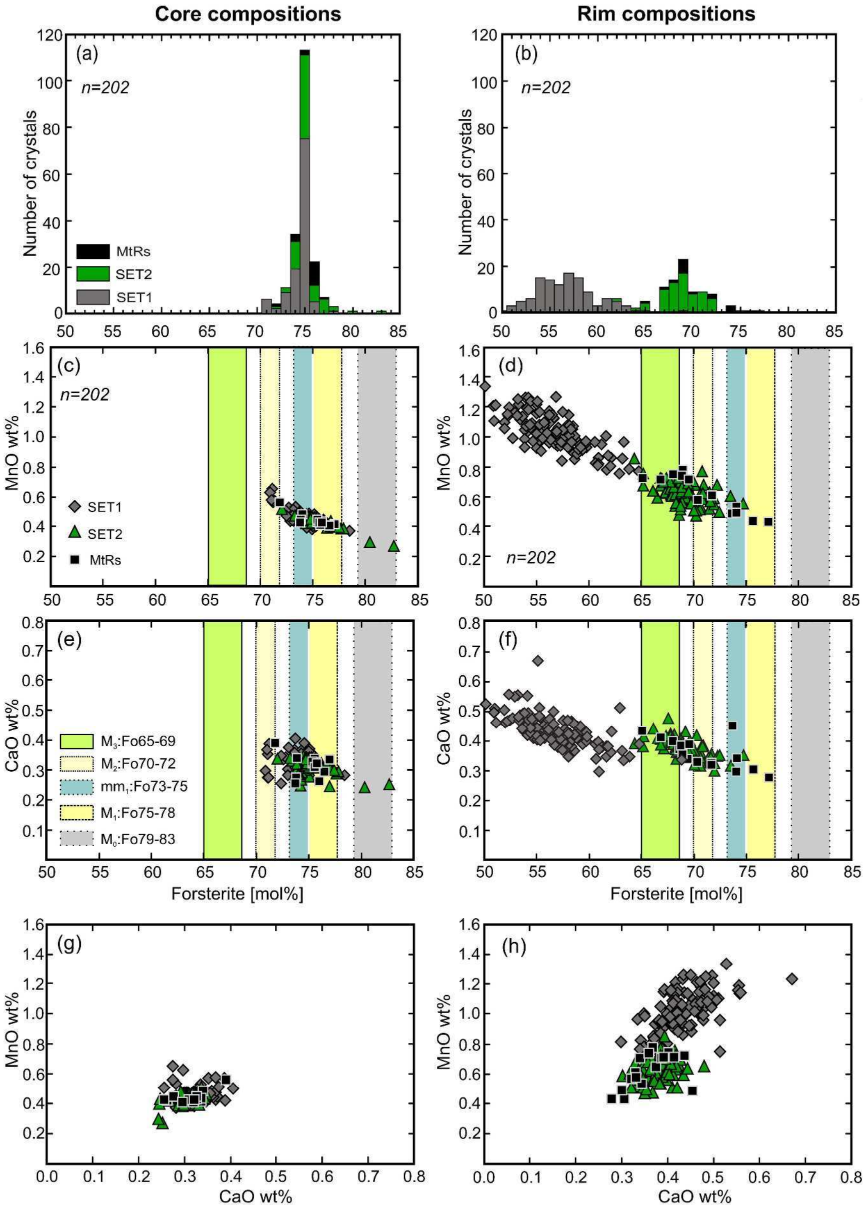

Figure 5

289x403mm (300 x 300 DPI)

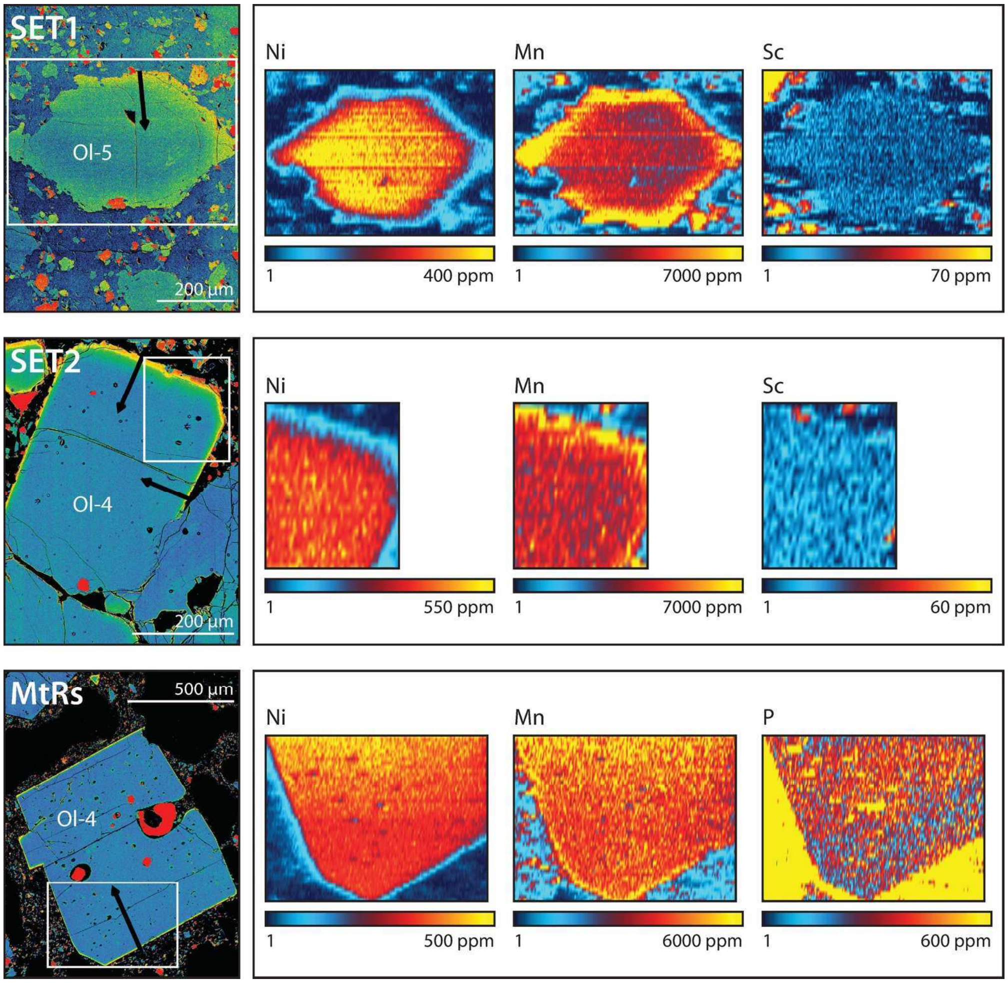

Figure 6

180x176mm (300 x 300 DPI)

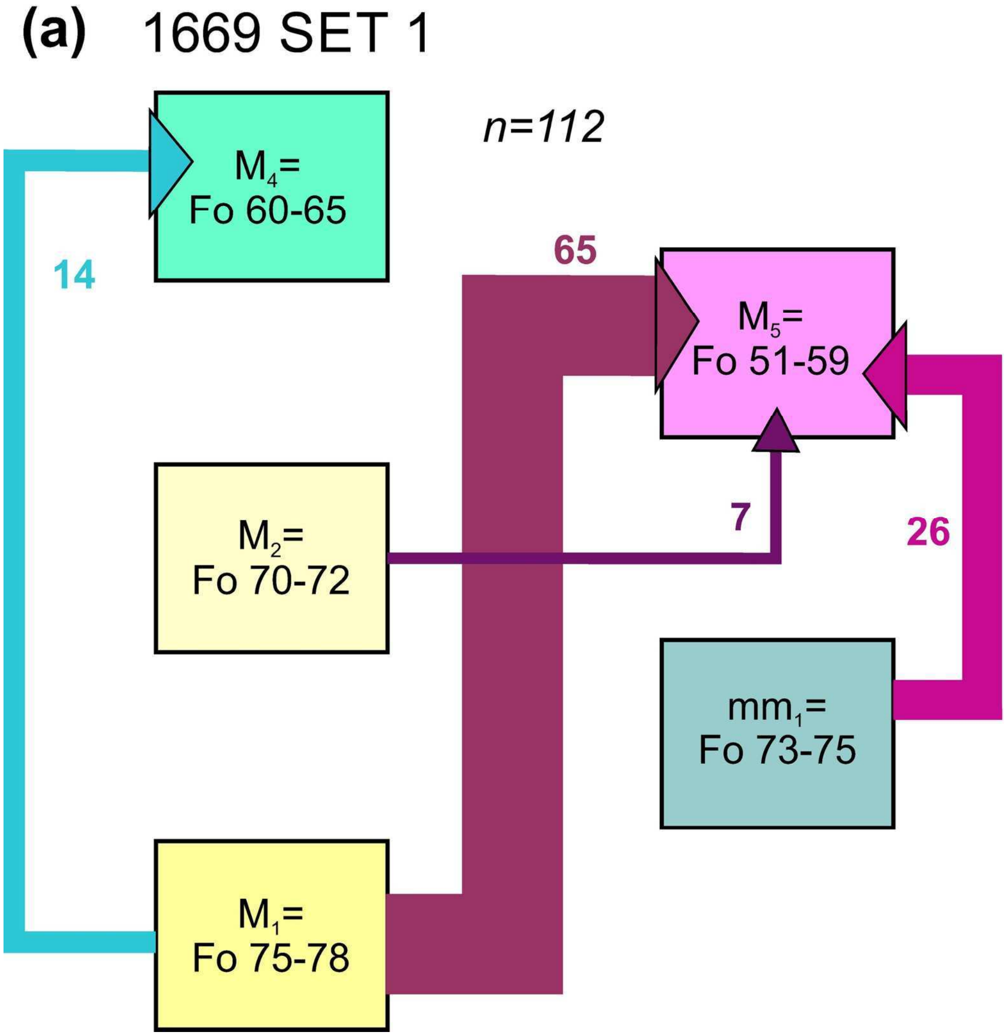

Figure 7a

163x168mm (300 x 300 DPI)

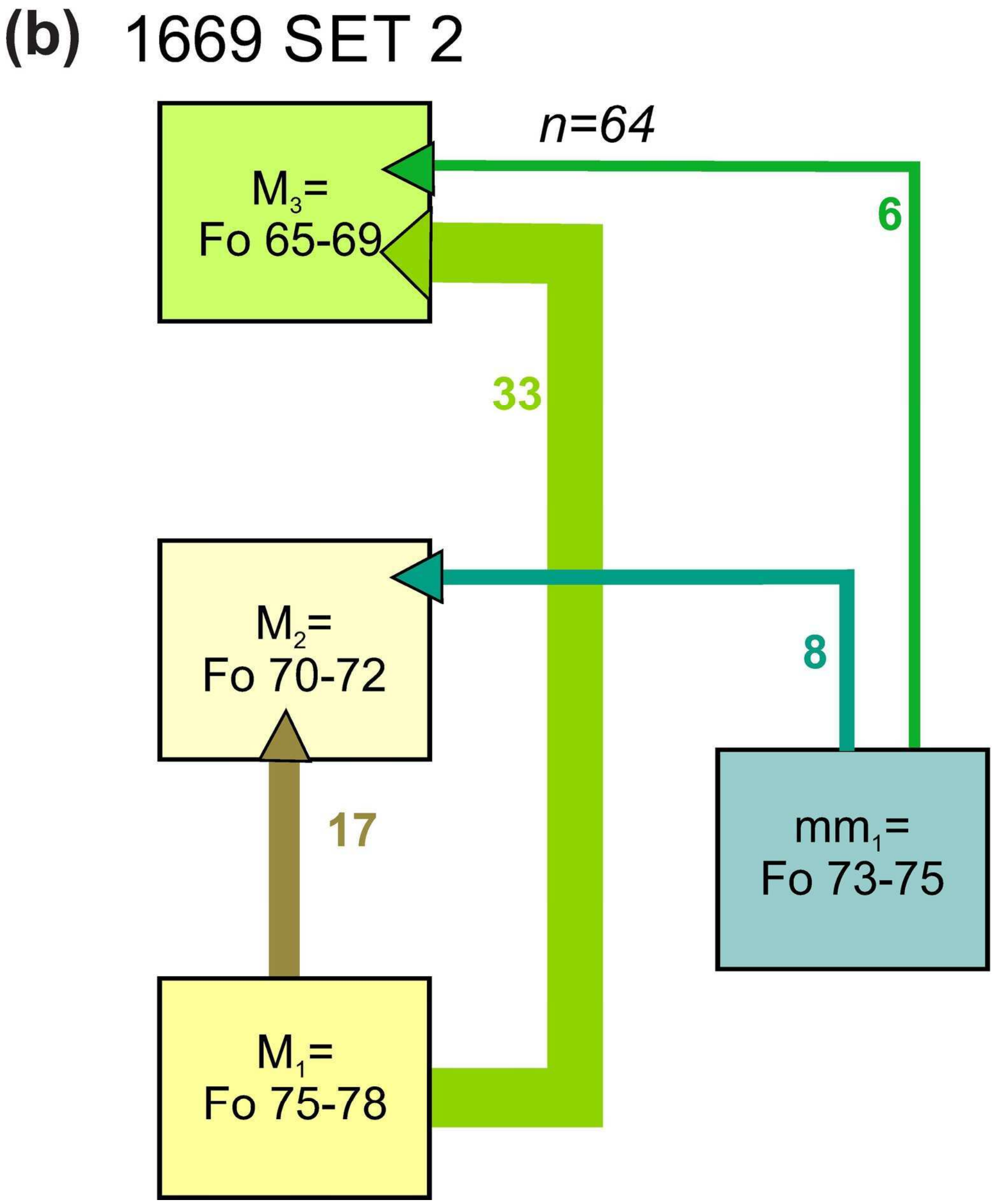

Figure 7b

163x197mm (300 x 300 DPI)

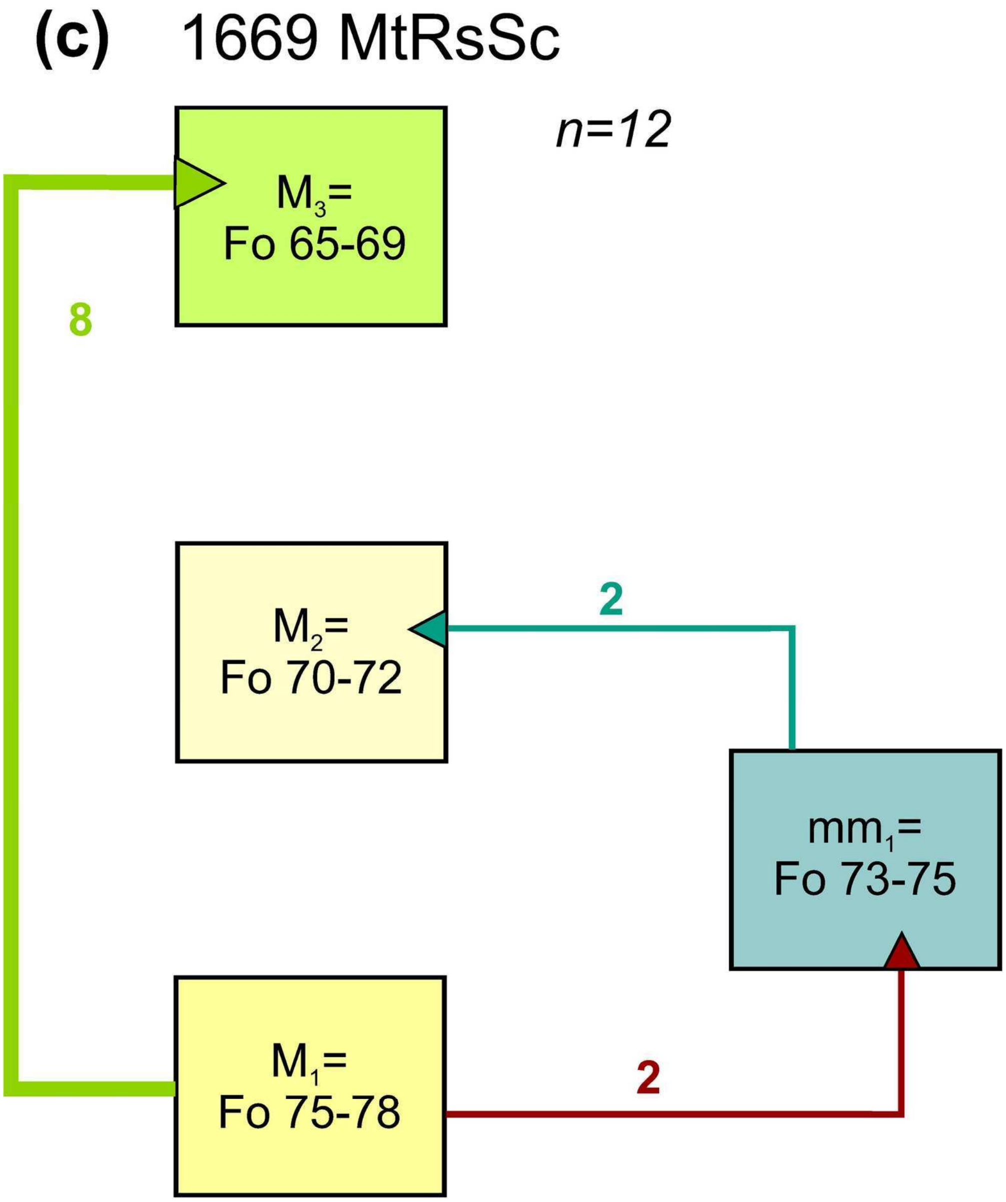

Figure 7c

163x195mm (300 x 300 DPI)

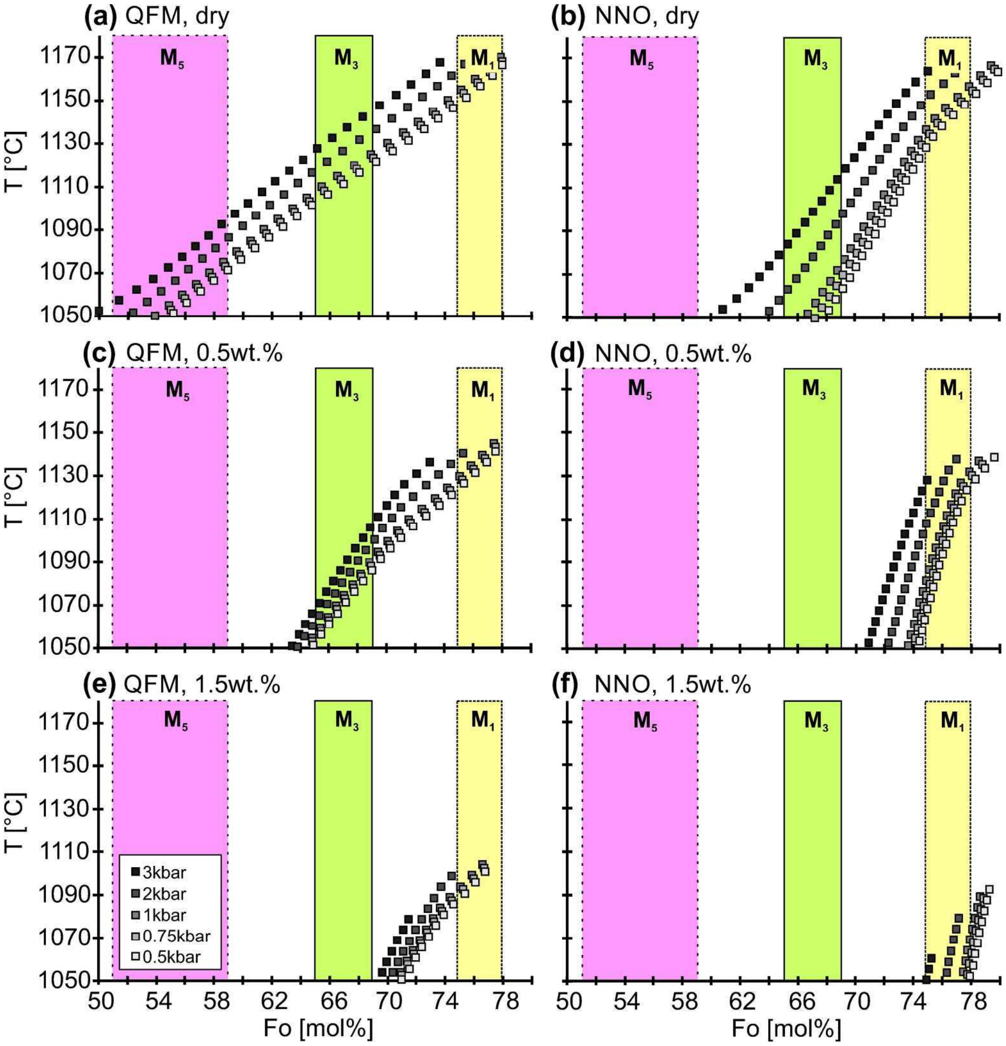

Figure 8

208x216mm (300 x 300 DPI)

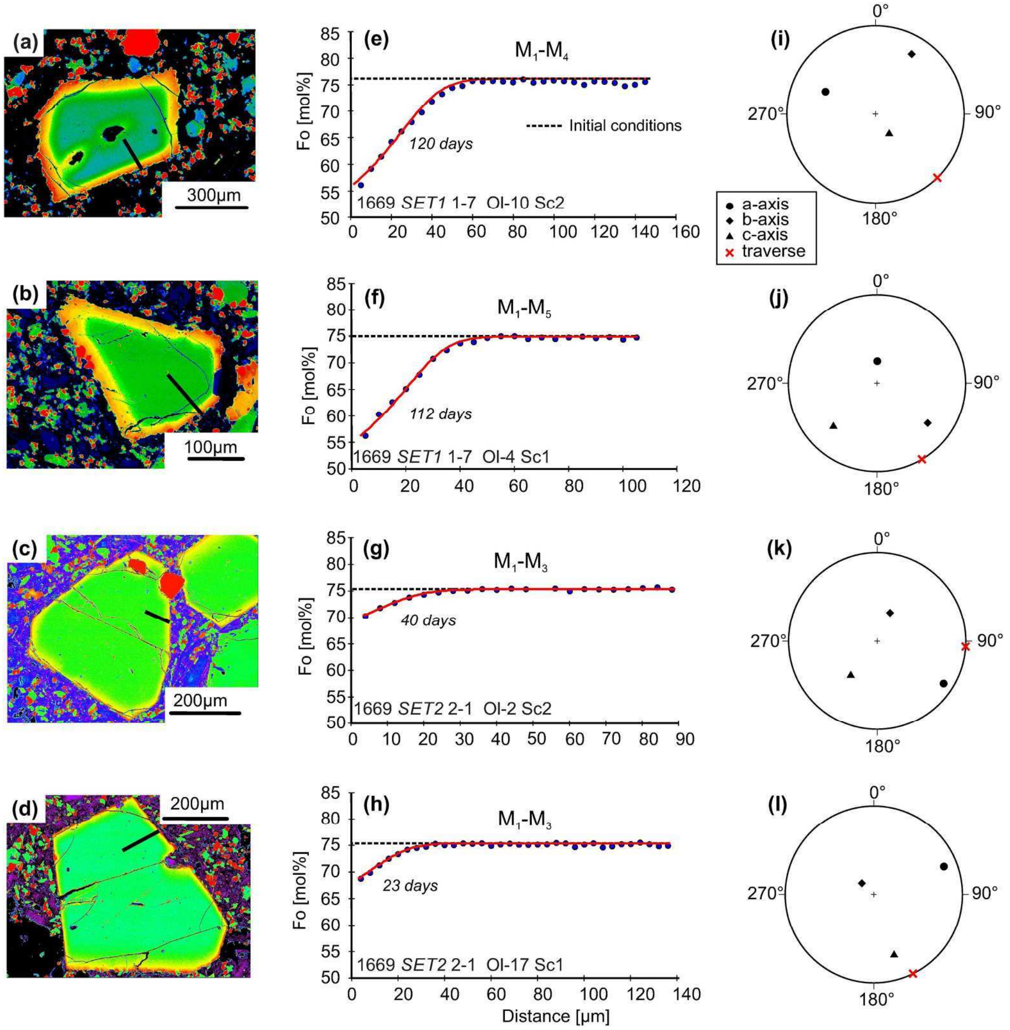

Figure 9

205x210mm (300 x 300 DPI)

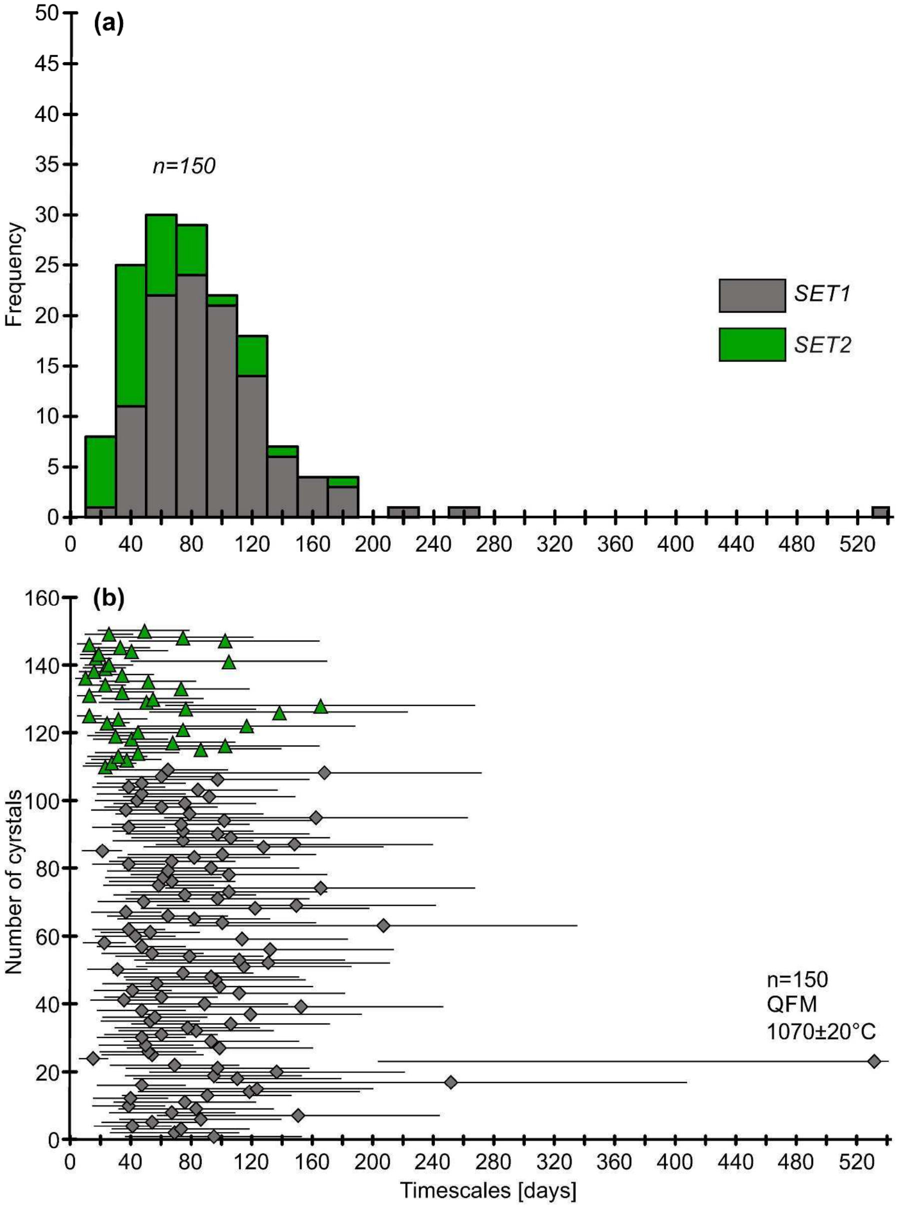

Figure 10

265x356mm (300 x 300 DPI)

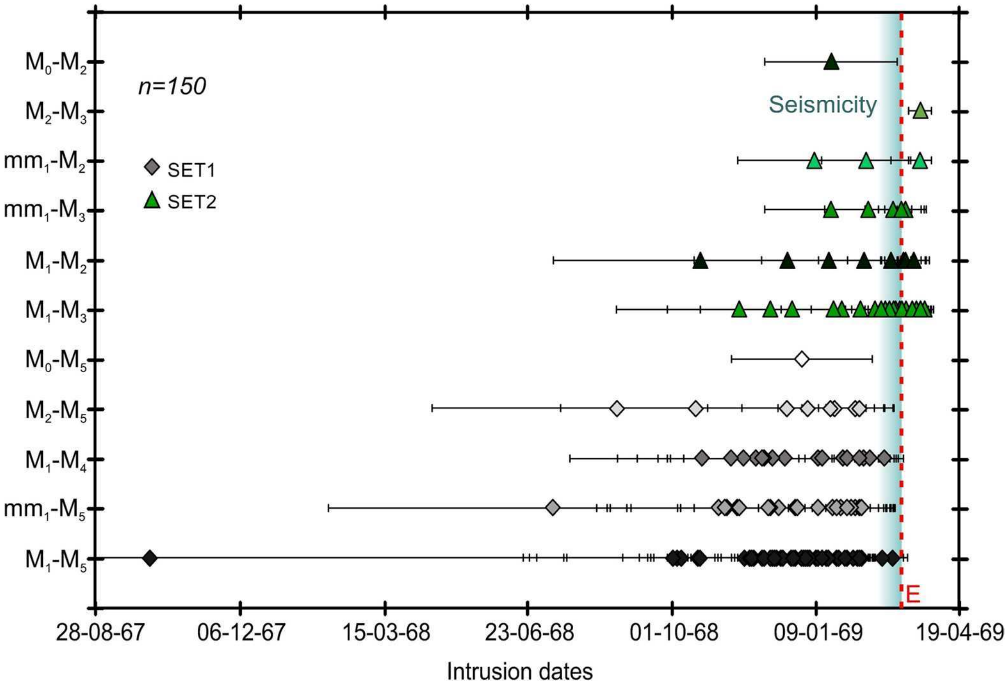

Figure 11

137x93mm (300 x 300 DPI)

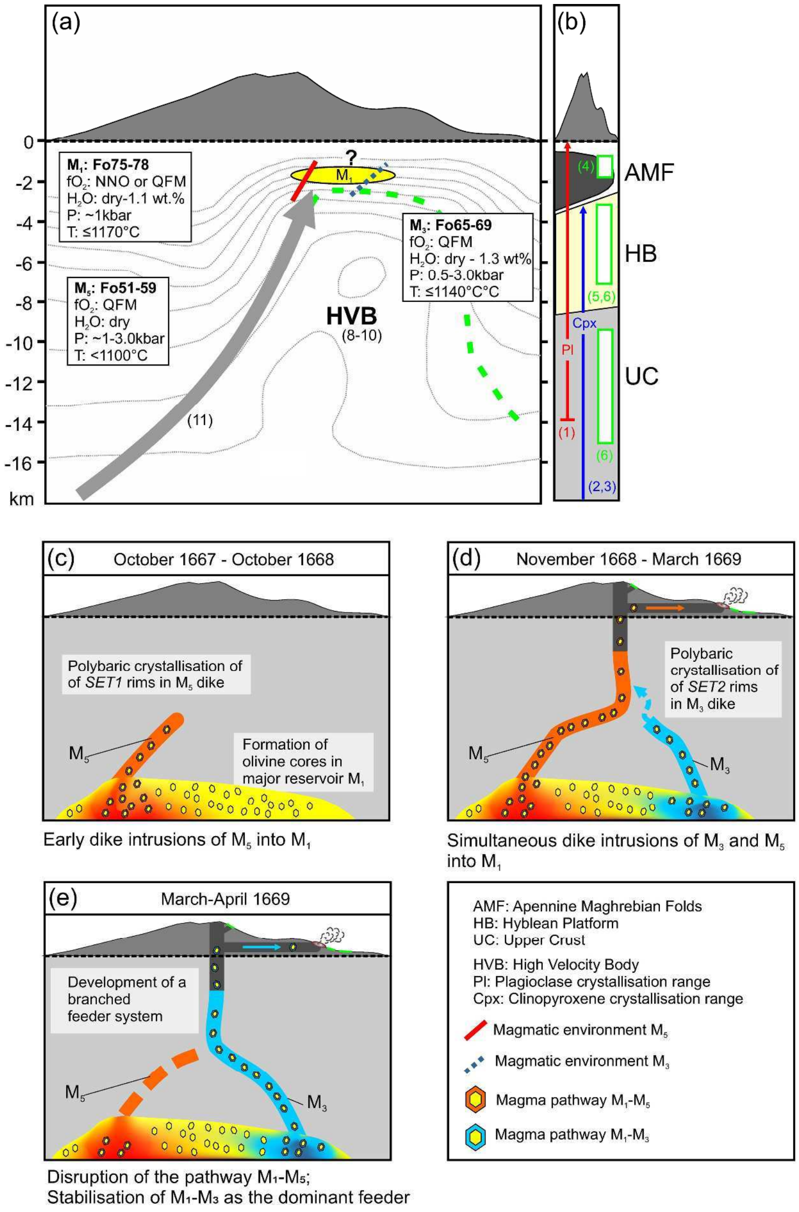

Early dike intrusions of M$_5$ into M$_1$

Simultaneous dike intrusions of M$_3$ and M$_5$ into M$_1$

Disruption of the pathway M$_1$-M$_5$;
Stabilisation of M$_1$-M$_3$ as the dominant feeder

Figure 12

279x423mm (300 x 300 DPI)

Table 1 Summary of 17th century flank activity

Flank eruption	**Location and notes**	**Volume and length**	**References**
1607 (June 28 - ?)	NW flank (2500-1500 m?); fissure above Monte Spagnolo cinder cone	Volume n.d.; lava flow of ~5 km	[1-3]
1610 (1st phase February 6 – May 3; 2nd phase May 3 – August 15)	1st phase: SSW flank (2800-2200 m); Grotta degli Archi craters; 2nd phase: SW flank (2300-1700 m); Large lava flows near Adrano	Total volume of lava flows: 120×10^6 m^3 (1st phase 30×10^6 m^3; 2nd phase 90×10^6 m^3); Total volume of pyroclastic material: $<4\times10^6$ m^3 (1st phase 3×10^6 m^3; 2nd phase $<1\times10^6$ m^3); Total length of lava flow field: 11 km	[1-4]
1614 (July 1) – 1624 (?)	N flank (~2500 m); most of the eruptive fissure is buried under younger lavas, but two larger cones (Due Pizzi) remain visible	Total volume of lava flows: ~1 km^3; Total volume of pyroclastic material: 2×10^6 m^3; Complex lava flow field up to ~9 km in length	[1-3]
~1630	NW flank from a fissure at 2250 m elevation, emitting "Val di Cannizzola" lava flow Another small lava flow located higher upslope was erupted from a fissure just below Punta Lucia.	n.d.	
1634 (December 18) – 1636 (June)	SE flank (2090-1975 m); short fissure forming a row of hornitos and lava flows causing damages in the area above Zafferana and threatens the village of Fleri	Total volume of lava flows: 180×10^6 m^3; Total volume of pyroclastic material: 1×10^6 m^3; Length lava flow field: ~9 km, divided into two branches	[4]; [1]; [2]; [3]
1643 (February)	NE flank (2000-1700-1380-1350-1250 m); this is probably one of the smallest flank eruptions of Etna characterized by a NE-SW and NNE-SSW fracture system that produced small lava flows	Total volume of lava flows: ~1×10^6 m^3 ?; Length of lava flows: up to ~5 km	[1-2]
1646 (November 20) – 1647 (January 17)	NNE flank (1950 m); intense Strombolian activity formed the Mt. Nero scoria cone, and lava flows causing damages to cultivated areas	Total volume of lava flows: 160×10^6 m^3; total volume of pyroclastic material: 7×10^6 m^3; lava flow up to ~7 km long	[1-3]; [5]
1651 (January 17) – 1653 (?)	W flank (2500-2120 m); lava flows partially destroys Bronte and causes damage. The lava flow-field has many areas of ropy pahoehoe, a	Total volume of lava flows (only western flank): 500×10^6 m^3; lava flow field	[6]; [2]; [3]

	rather rare lava type on Etna. An eruption is also reported to have occurred in 1651 on the eastern flank (Macchia di Giarre) and was covered by the 1689 lava	up to ~14 km long	
1669 (March 11 – July 11)	S Flank (850-700 m); development of a NNW-SSE-oriented fracture system 14-km-long (from Mt. Frumento Supino, 2800 m to Mompilieri, 600 m). Vigorous Strombolian activity formed the Mts. Rossi scoria cones. Lava effusions divided into three main branches that destroyed La Guardia, Belpasso, Mompilieri, Camporotondo, S. Pietro Clarenza, Massa Annunziata, S. Giovanni Galermo, Misterbianco and the western part of Catania	Total volume of lava flows: $>600\times10^6$ m^3; total volume of pyroclastic material: from 80 to 250×10^6 m^3; lava flow field up to ~17 km long covering an area of 40 km^2	[1-3]; [6]; [7]; [8]; [9];

n.d.: not determined; [1] Recupero (1815); [2] Branca & Del Carlo (2004); [3] Tanguy *et al.* (2007); [4] Carrera (1636); [5] Ferrara (1818); [6] Mancino (1669); [7] Borelli (1670); [8] Branca *et al.* (2015); [9] Mulas *et al.* (2016)

Table 2 Sample locations

	Sample	Latitude (N)	Longitude (E)	Location	Notes
SET1	1-6	37.550439°	14.986601°	Piano Tavola	samples of lava emitted on March 19, 1669
	1-7	37.550313°	14.988188°	Piano Tavola	samples of lava emitted on March 19, 1669
	1-8	37.549912°	14.988487°	Piano Tavola	samples of lava emitted on March 19, 1669
	1-9	37.549524°	14.987525°	Piano Tavola	samples of lava emitted on March 19, 1669
	1-10	37.549245°	14.986397°	Piano Tavola	samples of lava emitted on March 19, 1669
SET2	2-1	37.515367°	15.041863°	Catania San Nullo	samples of lava emitted after March 29 (possibly April 04) 1669
	2-2	37.516550°	15.041239°	Catania San Nullo	samples of lava emitted after March 29 (possibly April 04) 1669
	2-3	37.515609°	15.043251°	Catania San Nullo	samples of lava emitted after March 29 (possibly April 04) 1669
	2-4	37.514929°	15.043315°	Catania San Nullo	samples of lava emitted after March 29 (possibly April 04) 1669
	2-5	37.514670°	15.042788°	Catania San Nullo	samples of lava emitted after March 20 (possibly April 04) 1669
	MtRs	37.61924°	15.01103°	Monte Rossi scoria cone	Monte Rossi scoria cone bomb erupted after March 20 (possibly March 25) 1669

Table 3 Bulk rock compositions of SET1 and SET2 eruption products

	SET1				**SET2**				**MtRs**
Oxide (wt%)	**1-6**	**1-7**	**1-8**	**1-9**	**2-1**	**2-2**	**2-3**	**2-4**	**MtRs**
SiO_2	48.59	48.52	48.55	48.52	48.81	48.79	48.84	48.86	48.57
TiO_2	1.46	1.48	1.47	1.48	1.51	1.51	1.52	1.50	1.60
Al_2O_3	18.02	18.01	17.87	17.96	18.43	17.98	18.03	18.13	18.25
Fe_2O_3	10.09	10.06	10.07	10.04	10.17	10.27	10.37	10.28	10.72
FeO	9.08	9.05	9.06	9.03	9.15	9.24	9.33	9.25	9.65
CaO	10.47	10.47	10.54	10.58	10.12	10.56	10.32	10.44	10.40
MgO	5.23	5.05	5.23	5.11	4.73	5.17	5.07	5.13	5.06
MnO	0.17	0.17	0.17	0.17	0.17	0.17	0.17	0.17	0.19
K_2O	1.45	1.46	1.41	1.47	1.57	1.46	1.52	1.49	1.32
Na_2O	3.67	3.72	3.64	3.68	3.84	3.70	3.71	3.71	2.77
P_2O_5	0.50	0.51	0.50	0.51	0.54	0.52	0.53	0.52	0.51
Total	99.59	99.36	99.53	99.42	100.48	99.53	100.34	100.44	100.66
LOI	*-0.29*	*-0.32*	*-0.15*	*-0.33*	*-0.32*	*0.12*	*0.03*	*-0.03*	*1.27*
Rb (ppm)	36	35	30	33	34	33	32	36	27
Ba (ppm)	768	773	701	712	737	782	713	780	764
Th (ppm)	33	33	27	27	28	34	29	34	39
U (ppm)	<20	<20	<20	<20	<20	<20	<20	<20	<20
Nb (ppm)	50	53	47	46	49	53	51	54	59
La (ppm)	75	87	87	66	79	81	80	86	80
Ce (ppm)	135	123	118	132	126	131	133	131	138
Pb (ppm)	30	22	19	17	20	20	21	20	18
Sr (ppm)	1171	1183	1161	1169	1205	1166	1172	1178	1251
Nd (ppm)	44	53	49	47	50	47	47	51	49
Zr (ppm)	211	216	215	215	225	220	223	219	241
Y (ppm)	27	27	25	23	25	28	25	28	31
Ni (ppm)	31	33	32	30	30	31	34	47	34
Cr (ppm)	52	48	57	47	40	47	44	67	43
V (ppm)	253	259	245	227	238	260	252	261	292
Co (ppm)	31	31	28	27	28	32	28	31	34
Cu (ppm)	127	134	94	107	115	120	112	132	140
Zn (ppm)	91	94	84	80	84	99	94	97	110

Notes: LOI: Loss on ignition; Note that the MtRs sample has a high LOI, which is not untypical for scoria.

Table 4 Comprehensive timescale record of *SET1* and *SET2* olivines

Sample	Olivine	Timescale [days]	1σ	Sequence of reservoirs
1-6	Ol-1	95	59	mm1-M5
	Ol-3	69	43	M1-M5
	Ol-4	73	45	M1-M5
	Ol-19	42	26	mm1-M5
	Ol-16	55	34	M1-M5
	Ol-11	86	53	M1-M5
	Ol-13	151	93	M1-M5
	Ol-12b	68	42	M1-M4
	Ol-14	84	52	mm1-M5
	Ol-28	39	24	mm1-M5
	Ol-27	76	47	M1-M5
	Ol-24	40	25	M1-M5
	Ol-30	91	56	M1-M4
	Ol-6	119	73	M1-M5
	Ol-8	124	76	mm1-M5
	Ol-9	48	29	M1-M5
	Ol-5	252	156	mm1-M5
	Ol-29	111	68	M1-M4
	Ol-22	95	59	mm1-M5
	Ol-23	137	84	mm1-M5
	Ol-25	98	60	M1-M5
	Ol-31	69	43	M1-M5
	Ol-7	531	328	M1-M5
1-7	Ol-23	16	10	M1-M5
	Ol-22	55	34	M1-M5
	Ol-21	52	32	mm1-M5
	Ol-20	99	61	M1-M4
	Ol-19	50	31	M1-M4
	Ol-18	94	58	M1-M5
	Ol-16	48	29	M1-M4
	Ol-17	60	37	M1-M5
	Ol-15b	84	52	M1-M5
	Ol-14	78	48	M1-M5
	Ol-13	107	66	M1-M5
	Ol-12	53	33	M1-M5
	Ol-11	56	35	M2-M5
	Ol-10	120	74	M1-M4
	Ol-9a	48	29	M1-M5
	Ol-8b	153	94	M2-M5
	Ol-8a	89	55	M2-M5

Table 4 cont.

Sample	Olivine	Timescale [days]	1σ	Sequence of reservoirs
1-7	Ol-7	36	22	M1-M4
	Ol-6	60	37	M1-M5
	Ol-4	112	69	M1-M5
	Ol-3	42	26	M2-M5
	Ol-2a	99	61	M1-M5
	Ol-1	58	36	mm1-M5
	Ol-24	96	60	M1-M5
	Ol-25	94	58	M1-M5
	Ol-2c	75	46	M1-M5
	Ol-2d	32	20	M1-M4
1-8	Ol-19	115	71	M1-M5
	Ol-18	131	81	mm1-M5
	Ol-17	112	69	M1-M5
	Ol-16	79	49	M0-M5
	Ol-15	55	34	mm1-M5
	Ol-14	132	82	mm1-M5
	Ol-13	48	29	M1-M5
	Ol-11	23	14	M1-M5
	Ol-12	114	70	M1-M5
	Ol-10	43	27	M1-M5
	O-l9	53	33	M1-M5
	Ol-7	39	24	M2-M5
	Ol-6	207	128	M2-M5
	Ol-5	101	62	M1-M5
	Ol-4	82	51	mm1-M5
	Ol-3	65	40	M1-M5
	Ol-2	37	23	mm1-M5
	Ol-1	122	76	mm1-M5
1-9	Ol-1	150	92	M1-M5
	Ol-22	49	30	M1-M5
	Ol-18	98	60	M1-M5
	Ol-14	76	47	M1-M5
	Ol-21	105	65	M1-M5
	Ol-20	166	102	M1-M5
	Ol-24	59	36	M2-M5
	Ol-19	68	42	mm1-M5
	Ol-17	62	38	M1-M5
	Ol-8	105	65	M1-M4
	Ol-12	65	40	M1-M4
	Ol-7a	94	58	M1-M5

Table 4 cont.

Sample	Olivine	Timescale [days]	1σ	Sequence of reservoirs
1-9 cont.	Ol-7b	39	39	M1-M4
	Ol-4	68	68	M1-M5
	Ol-6	82	82	mm1-M5
	Ol-2	101	101	mm1-M5
	Ol-10	22	22	M1-M4
	Ol-11	128	128	M1-M4
	Ol-16	148	148	M1-M4
	Ol-5	75	75	M2-M5
	Ol-7c	107	107	M1-M4
1-10	Ol-21b	98	60	M1-M5
	Ol-20a	75	46	M1-M5
	Ol-20b	39	24	M1-M5
	Ol-18	73	45	M1-M5
	Ol-17	102	63	mm1-M5
	Ol-15	163	100	M1-M5
	Ol-14	79	49	M1-M5
	Ol-13	37	23	M1-M5
	Ol-11	60	37	M1-M5
	Ol-10	76	47	M1-M5
	Ol-9a	45	28	mm1-M5
	Ol-8	92	57	M1-M5
	Ol-6	48	29	mm1-M5
	Ol-5a	85	52	M1-M5
	Ol-4	39	24	M1-M5
	Ol-2	48	29	mm1-M5
	Ol-1a	98	60	M1-M5
	Ol-1b	60	37	M1-M5
	Ol-12	168	104	M1-M5
	Ol-22	65	40	M1-M5
2-1	Ol-17	23	14	M1-M3
	Ol-15	27	17	M1-M3
	Ol-8	37	23	M1-M3
	Ol-7	32	20	mm1-M3
	Ol-6a	45	28	M1-M3
	Ol-5	86	53	mm1-M2
	Ol-4	102	63	M1-M3
	Ol-3	68	42	M1-M3
	Ol-2	40	25	M1-M3
	Ol-1	30	19	M1-M3

2-2	Ol-15	45	28	M1-M3
	Ol-12	75	46	mm1-M3
	Ol-11	117	72	M1-M3
	Ol-10	24	15	M1-M2
	Ol-7	32	20	M1-M3
	Ol-5	13	8	mm1-M2
	Ol-14	138	85	M1-M3
2-3	Ol-2a	76	47	M1-M2
	Ol-2b	166	102	M1-M2
	Ol-3	50	31	mm1-M2
	Ol-5	55	34	M1-M3
	Ol-6	13	8	M2-M3
2-4	Ol-23	35	21	M1-M3
	Ol-20	73	45	M1-M3
	Ol-19	23	14	M1-M2
	Ol-18	52	32	M1-M2
	Ol-17	10	6	M1-M3
	Ol-14	35	21	M1-M3
	Ol-9	16	10	M1-M3
	Ol-8	23	14	mm1-M3
	Ol-7	26	16	M1-M3
	Ol-6b	105	65	M1-M2
	Ol-6a	17	11	M1-M2
	Ol-4	19	12	M1-M3
	Ol-2	40	25	M1-M3
	Ol-1	33	20	M1-M2
2-5	Ol-3	13	8	M1-M3
	Ol-12	102	63	M1-M3
	Ol-11	75	46	M0-M2
	Ol-7	26	16	mm1-M3
	Ol-5	49	30	mm1-M3